Satellite Products and Services Review Board

VIIRS NDE Surface Albedo Algorithm Theoretical Basis Document

Shunlin Liang, Dongdong Wang, Yuan Zhou
University of Maryland, College Park
Yunyue Yu, Jingjing Peng
NOAA/NESDIS/STAR

Version 1.3

July, 2018

TITLE: VIIRS NDE SURFACE ALBEDO ALGORITHM THEORETICAL BASIS DOCUMENT VERSION 1.3

AUTHORS:

Shunlin Liang, Dongdong Wang, Yuan Zhou
University of Maryland, College Park

Yunyue Yu, Jingjing Peng
NOAA/NESDIS/STAR

DOCUMENT HISTORY
DOCUMENT REVISION LOG

The Document Revision Log identifies the series of revisions to this document since the baseline release. Please refer to the above page for version number information.

DOCUMENT TITLE: VIIRS Surface Albedo Algorithm Theoretical Basis Document			
DOCUMENT CHANGE HISTORY			
Revision No.	**Date**	**Revision Originator Project Group**	**CCR Approval # and Date**
1.0	10/31/2017	Developing a New ATBD Document	
1.1	3/16/2018	Updates according to ARR	August 2010
1.2	3/22/2018	Updates according to ARR	
1.3	7/20/2018	Updates according to Beta Maturity Review of N20 VIIRS Albedo	

LIST OF CHANGES

Significant alterations made to this document are annotated in the List of Changes table.

DOCUMENT TITLE: VIIRS Surface Albedo Algorithm Theoretical Basis Document					
LIST OF CHANGE-AFFECTED PAGES/SECTIONS/APPENDICES					
Version Number	**Date**	**Changed By**	**Page**	**Section**	**Description of Change(s)**
1.1	03/16/18	D. Wang			Following new template to revise the ATBD
1.2	03/22/18	J. Peng			Updated Product Requirements, Instrument Description and Quality Diagnostics
1.3	07/23/18	J. Peng			Updated the sea-ice albedo algorithm and Revised the whole document

TABLE OF CONTENTS

LIST OF FIGURES AND TABLES

Page

1. INTRODUCTION

Surface broadband albedo is loosely defined as the ratio between upwelling and downwelling shortwave radiation (Liang 2004). It represents the reflectivity of a surface under the actual illuminating condition. To distinguish it from other types of albedo, this albedo is usually called apparent albedo or blue-sky albedo (Liang et al. 1999).Surface albedo is closely related to surface bi-directional reflectance, which usually changes with illuminating and viewing angles. Surface reflectance is an intrinsic characteristic of the Earth surface, including land surfaces, which are the focus of this study. It is strongly dependent on land cover type and varies both spatially and temporally. Surface reflectance is a function of surface parameters such as vegetation type and abundance, soil type and moisture and so on. Because surface reflectance changes spectrally and angularly, values of broadband albedo also change with spectral and angular distributions of incident solar radiation. Thus, in addition to surface properties, apparent albedo is also dependent on atmospheric conditions and solar zenith angle (SZA). To simplify the dependency of albedo on SZA and atmosphere, two conceptual terms of albedo, white-sky and black-sky albedo, are frequently used (Lucht et al. 2000).

Historically, parameterizations of LSA were used in land and climate models, whereby LSA was computed as functions of land and atmospheric variables, such as land surface type, leaf area index, and SZA (Bonan et al. 2002). The spatial and temporal variability of LSA cannot be well captured by such simplified approaches. Spatially, land cover and land use determine the overall distribution pattern of LSA (Zhang et al. 2010). Temporally, many factors contribute to intra- and inter-annual variability of LSA. For example, LSA changes seasonally with vegetation phenology (Moody et al. 2005), seasonal snow (Kuusinen et al. 2012), and shift of SZA (Wang et al. 2005). Long-term changes in land surface features, such as from alteration of land use and land cover (Loarie et al. 2011), vegetation dynamics (Loranty et al. 2011), and changes in soil moisture (Zhu et al. 2011), will lead to inter-annual variations in LSA. Meanwhile, changes in LSA also feed back to climate. For instance, both models and observations suggest that a positive feedback exists between LSA and precipitation at regional scale (Eltahir 1998; Zheng and Eltahir 1998). Thus, long-term records of LSA are an irreplaceable resource for monitoring the variability of LSA and understanding its interaction with the climate system.

Remote sensing is a unique tool for mapping LSA globally on a regular basis. Attempts to generate global maps of LSA can be traced back to the early meteorological satellite Nimbus 3 (Raschke et al. 1973). Since then, a series of optical sensors have been applied to derive global data on LSA (Csiszar and Gutman 1999; Li and Garand 1994). The launch of the Moderate Resolution Imaging Spectroradiometer (MODIS) began a new era of monitoring LSA with satellites (Townshend and Justice 2002). The higher spatial resolution, better spectral configuration, and improved radiometric and geographic accuracy of MODIS facilitate a high-quality global albedo product at 8-day frequency (Schaaf et al. 2002). As its successor, the Visible Infrared Imaging Radiometer Suite (VIIRS) from the Suomi National

Polar-orbiting Partnership (Suomi NPP) and future Joint Polar Satellite System (JPSS) missions will furnish us with a continued opportunity to monitor LSA from space.

1.1. Product Overview

1.1.1. Product Description

The Interface Data Processing Segment (IDPS) VIIRS land surface albedo data is part of the VIIRS surface albedo Environmental Data Record (EDR). Although reliable albedo estimates have been reported for the valid pixels with clear-sky VIIRS observations, the current VIIRS granule albedo product suffers from several issues: (1) albedo values are only retrieved for clear-sky pixels and the product has a considerable number of data gaps; (2) the current algorithm estimates albedo from a single VIIRS observation and contains a certain extent of noise; (3) the albedo of the current product is an instantaneous value; (4) the sea-ice albedo retrieval failed.

To address these issues, we developed a two-step approach to produce a new daily granule and gap-filled product based on VIIRS data, which is implemented in the NDE framework. This NDE LSA product is a granule-based product, containing albedo parameter over land and sea-ice surfaces. A direct estimation algorithm was developed to estimate daily mean blue-sky albedo from clear-sky VIIRS observations over land pixels. The direct estimation algorithm uses TOA spectral reflectance data [known as VIIRS Sensor Data Record (SDR)] of nine VIIRS bands (M1, M2, M3, M4, M5, M7, M8, M10, and M11) as major inputs. A VIIRS cloud mask Intermediate Product (IP) helps to exclude cloudy-sky pixels. Land cover data, VIIRS ice concentration EDR, and snow mask EDR were used to determine the LUT type deployed on each pixel. There are four land type specified LUTs included in the algorithm: General, Desert, Snow, and Sea-ice. The VIIRS albedo granule data have been validated using field measurements. The accuracy is comparable to existing satellite albedo products.

The NDE LSA process consists of two components. The granule albedo is estimated online from a combination of the directly estimated albedo and a historical temporally filtered gap-free albedo; the historical albedo is derived offline using granule albedo previously obtained. The online direct estimation approach, which has been widely used for estimating land surface albedo from a variety of satellite data, is initially used to estimate daily mean blue-sky land surface albedo from clear-sky VIIRS data of TOA spectral reflectance. The offline statistical temporal filter is then applied to combine information from the albedo retrieved with observations of the current day (if existing) and the adjacent days as well as historical climatology to generate a gap-free and noise-reduced albedo data set.

1.1.2. Product Requirements

The requirements for the VIIRS NDE Surface Albedo are described in the Section 5.4.1 in JPSS Level 1 Requirements Supplement. (Refer to http://www.jpss.noaa.gov/technical_documents.html)

1.2. Satellite Instrument Description

The Surface Albedo uses data from Visible Infrared Imaging Radiometer Suite (VIIRS) instrument as input to the algorithm. The VIIRS instrument is a component of the Suomi National Polar-orbiting Partnership (NPP) satellite and of the Joint Polar Satellite System (JPSS) satellites. NPP was launched on 28 October 2011, and JPSS-1 (NOAA-20) was launched on November 18, 2017. JPSS is the latest generation of U.S. polar-orbiting environmental satellites, which cross the equator about 14 times daily in the afternoon orbit, providing full global coverage twice a day.

The VIIRS sensor was designed to improve the series of measurements initiated by the Advanced Very High Resolution Radiometer (AVHRR) and the Moderate Resolution Imaging Spectroradiometer (MODIS). VIIRS data is used to measure cloud and aerosol properties, land surface parameters including albedo. VIIRS data also servers to improve studies in global climate change.

The VIIRS instrument is a 'whiskbroom' radiometer, which collects radiometric and imagery data in 22 bands from 0.4 to 12.5 μm. Five of these channels are high-resolution imagery bands (I-bands), and sixteen are designed as moderate-resolution bands (M-bands). One of these M-bands is the Day/Night band (DNB), which is a panchromatic band sensitive to visible and near-infrared wavelengths. For further details please refer to the VIIRS Sensor Data Record (SDR) User's Guide (NOAA Technical Report NESDIS 142).

2. ALGORITHM DESCRIPTION

The implementation of this new gridded VIIRS albedo product consists of two major steps: direct retrieval and temporal filtering. The direct retrieval procedure is granule-driven and employs the improved direct estimation algorithm to generate daily mean albedo granule from VIIRS clear-sky SDR data. The albedo granule directly retrieved from the first step will then be gridded and converted to a sinusoidal map projection. The gridded data will serve as the input of the temporal filtering step. The temporal filtering process is tile-driven and executed at the end of each day, which mainly implements a statistical temporal filter algorithm to combine albedo from the current and temporally neighboring days and climatology information to generate a gap-filled and noise-reduced albedo product.

2.1. Processing Outline

The direct retrieval and temporal filtering algorithms are implemented into two separate modules in the software development. The online processing part employs the direct retrieval algorithm to generate Primary Surface Albedo ("VIIRS_Albedo_IP") from VIIRS clear-sky observations (Figure 2-1). Data gaps in the clear-sky albedo granule are then filled using the historical albedo information, which come from the temporal filtering algorithm (the offline processing part). The gap-filled albedo granule is also known as Improved Surface Albedo ("VIIRS_Albedo_EDR").

The offline processing part mainly implemented the temporal filtering algorithm with the albedo tiles gridded from Primary Surface Albedo during a 9-day window (precedent 8 days plus the current day) as the main input (Figure 2-2). The offline processing updates the historical albedo data that are used in the online processing part.

The input and output data of the online and offline processing parts will be summarized in the following section.
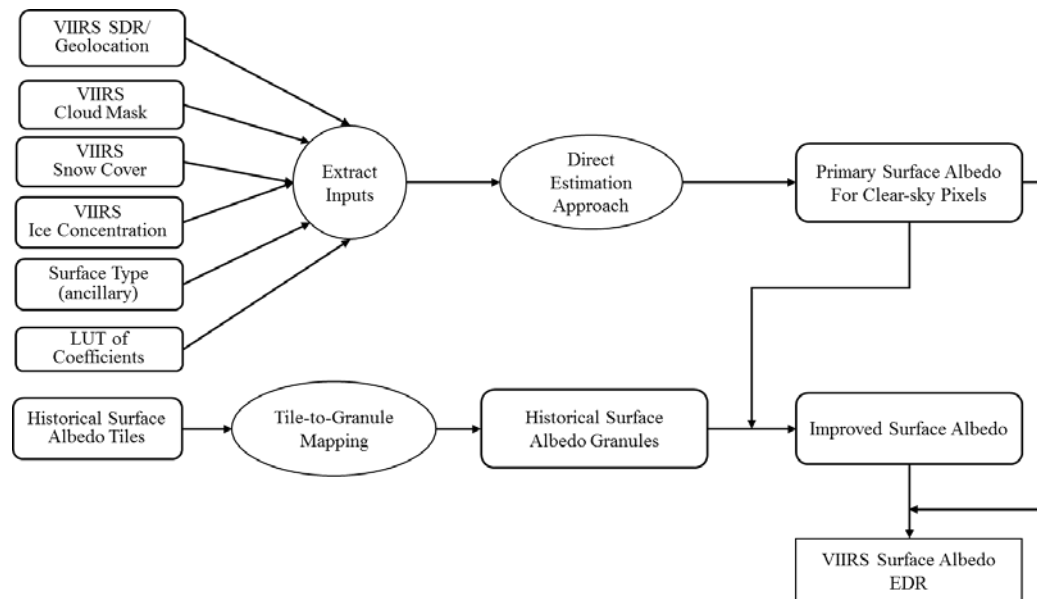
Figure 2-1. Software architecture for the online processing part.
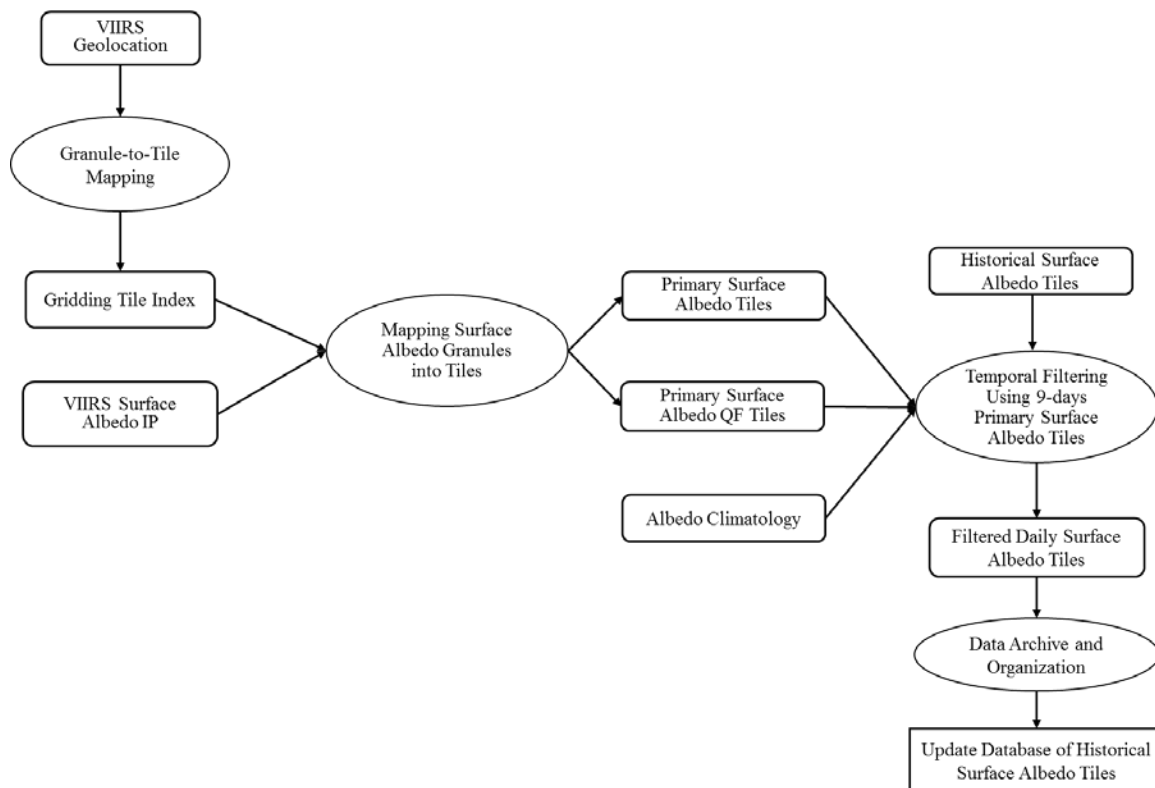
Figure 2-2. Software architecture for the offline processing part.

2.2. Algorithm Input

The online and offline parts use different input and output and are described separately. The required inputs for the online processing of NDE Surface Albedo algorithm unit are listed in Table 2-1, while that of the offline processing is listed in Table 2-2.

Table 2-1. Inputs required by the online processing of the NDE surface albedo algorithm unit

Input Data	Source	Description
VIIRS SDR	NDE	VIIRS gap-filled and converted M band SDR data (M1, M2, M3, M4, M5, M7, M8, M10, and M11)
VIIRS Geolocation	NDE	VIIRS terrain corrected geolocation data
Surface Type	NDE	Surface type mask at 1km resolution
VIIRS Cloud Mask	NDE	Cloud Mask produced by the Enterprise cloud mask algorithm
VIIRS Snow Mask	NDE	Snow Mask produced by the Enterprise Snow cover algorithm
VIIRS Ice Concentration	NDE	Ice Mask produced by the Enterprise Ice Concentration algorithm
Historical Surface Albedo Tiles	NDE	Filtered surface albedo tiles from (day-2) offline processing
Albedo Regression Coefficient LUT	DAP	Regression coefficients in multiangular bins linking TOA reflectance to albedo for various surfaces (General, Desert, Snow, Sea-ice)

Table 2-2. Inputs required by the offline processing of the NDE surface albedo algorithm unit

Input Data	Source	Description
VIIRS Surface Albedo IP	NDE	Current daytime (day+0) VIIRS Surface Albedo IP produced from online processing
VIIRS Geolocation	NDE	VIIRS terrain corrected geolocation data
Albedo Climatology	DAP	Prior knowledge of time-series surface albedo for offline filtering algorithm

2.3. Theoretical Description

The algorithm consists of two major steps: direct retrieval and temporal filtering. The direct retrieval procedure is granule-driven and employs the improved direct estimation algorithm to generate daily mean albedo granule from VIIRS clear-sky SDR data. The albedo granule directly retrieved from the first step will then be gridded and converted to a sinusoidal map projection. The gridded data will serve as the input of the temporal filtering step. The temporal filtering process is tile-driven and executed at the end of each day, which mainly implements

a statistical temporal filter algorithm to combine albedo from the current and temporally neighboring days and climatology information to generate a gap-filled and noise-reduced albedo product.

2.3.1 Direct Estimation Approach

Land surface albedo and sea-ice surface albedo are retrieved with different approaches. Their theoretical basis is discussed separately here.

2.3.1.1 Land Surface Albedo

The direct estimation method seeks to directly retrieve daily albedo over land surfaces from VIIRS observations (TOA reflectance) through modeling the relationship between surface albedo and TOA reflectance (Wang et al. 2017). Instead of leaving the integration process of surface incident radiation and albedo to the end user, the direct estimation method pre-calculates the integral values of daily mean albedo for various cases of atmospheric and surface conditions by modeling the atmospheric radiative transfer with a comprehensive database of atmospheric and surface parameters as inputs. Representative datasets of daily albedo and TOA reflectance are generated from the model simulation and used to train the regression models. These models will then be applied to VIIRS data to retrieve daily albedo. The direct estimation method includes the temporally explicit integration in the process of model construction so that end users of surface radiation budget can directly use products of daily albedo without the need to carry out complex computations on their own.

Two software packages, MODTRAN5 (Berk et al. 2004) and 6S (Kotchenova et al. 2008), were used to model atmospheric radiative transfer. The 6S software was mainly used for simulating TOA reflectance with consideration of surface BRDF. Direct and diffuse downward shortwave radiations under various SZA and atmospheric conditions were simulated by MODTRAN5. Because albedo is only retrieved from clear-sky observations, variations of aerosol are the major consideration for atmospheric parameters. Four aerosol types (including continental, urban, desert, and biomass burning aerosol) with nine optical depths (0.01, 0.05, 0.1, 0.15, 0.2, 0.3, 0.4, 0.5, and 0.6) were used as parameters for radiative transfer models.

Regarding the inputs of surface reflectance, two schemas (BRDF and Lambertian) were tested in this study. In theory, a database of spectral BRDF and broadband albedo is ideal for such studies. However, the corresponding data of broadband albedo for the spectral BRDF are usually calculated from narrowband albedo using empirical narrow-to-broadband conversion coefficients (Liang 2001). Insufficient spectral information in the BRDF database can be a source of uncertainties in estimating daily values of broadband albedo. In contrast, the library of surface spectra contains complete spectral information, though it does not consider the anisotropy of surface reflectance. To compare the relative importance of spectral and angular information for estimating daily albedo, we used both the surface BRDF database and surface spectra library as inputs for radiative transfer simulations. The BRDF

data were obtained from the MODIS BRDF product and converted to VIIRS bands (Wang et al. 2013). The spectra library was derived from the Advanced Spaceborne Thermal Emission and Reflection Radiometer (ASTER) (Baldridge et al. 2009) and the U.S. Geological Survey (USGS) (Clark 2007) surface spectra database.

With atmospheric and surface inputs available, simulating TOA reflectance using the 6S model for various viewing geometries is a straightforward process. An interval of 5° was used for view zenith angle (VZA) and SZA. Relative azimuth angle (RAA) increased in 10° intervals, although a smaller interval (5°) was used for cases near the principal plane (±20°). The rest of this section mainly focuses on simulation of daily albedo.

The diurnal trajectory of incident diffuse and direct solar radiation is needed for computing daily albedo from white-sky albedo and instantaneous black-sky albedo. For clear-sky days, the incident solar radiation and its diffuse partition are mainly dependent on aerosol and SZA. Changes of incident diffuse and direct solar radiation are simulated by MODTRAN5 and stored in a lookup table (LUT) for future use. In the current algorithm, the aerosol parameters are assumed to remain unchanged for the period of one day. It should be noted that aerosol loadings as well as cloud coverage will hardly stay constant during a day, which is a source of uncertainty in estimating daily albedo from one single satellite observation. Trajectory of SZA during one day can easily be calculated from time of day using the following equation:

$$\theta_s = \arccos[\sin\varphi\sin\delta + \cos\varphi\cos\delta\cos(\frac{t-12}{12}180)]$$

(1)

where φ is latitude, δ is the declination angle of the Earth, and t is the local time. The declination angle δ can be calculated from day of year (DOY) as:

$$\delta = 23.45\sin(360\frac{283+DOY}{365})$$

(2)

With Eqs. (1) and (2), SZA can be calculated for 30-min intervals for a given DOY and latitude. At these time points t_i, incident diffuse radiation $S_{diff}\downarrow(t_i)$ and direct radiation $S_{dir}\downarrow(t_i)$ is obtained by interpolating the pre-stored LUT of solar radiation. White-sky and black-sky albedo can both be easily calculated from BRDF kernel parameters with pre-integrated coefficients (Schaaf et al. 2002). Examples of diurnal changes of black-, white-, and blue-sky albedo for three surface types are illustrated in Figure 2-3.
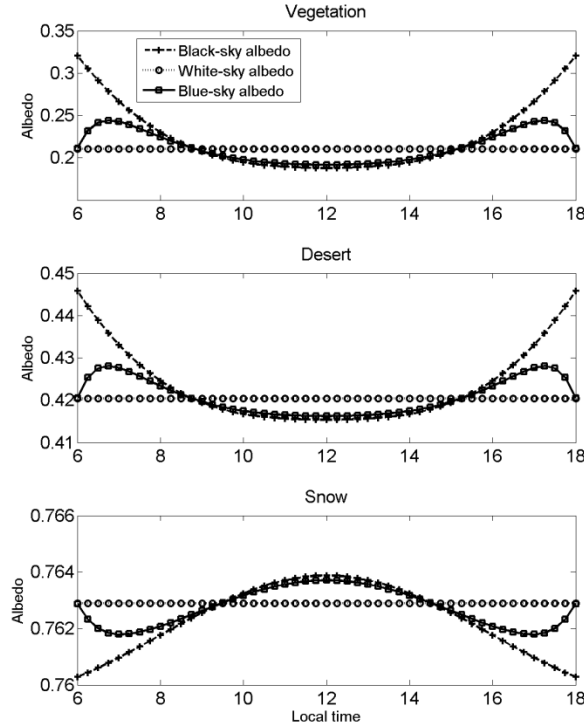
Figure 2-3. Examples of diurnal curves of black-, white- and blue-sky albedo values for three surface types.

From the discrete form of Eq. (5), daily mean albedo can be calculated as follows:

$$a_D = \frac{\sum\limits_{i \in Daytime}[S_{dir}\downarrow(t_i)a_{bs}(t_i) + S_{diff}\downarrow(t_i)a_{ws}]}{\sum\limits_{i \in Daytime}S\downarrow(t_i)}$$

(3)

Thus, a daily mean value of surface broadband blue-sky albedo can be calculated for one case of surface reflectance, aerosol, latitude, and day of year. Together with the TOA spectral reflectance simulated earlier, the training data to model daily albedo from TOA spectral reflectance are now complete. The training data were binned by viewing geometry, latitude, and declination angle. For each bin, a group of daily albedo together with its corresponding TOA reflectance for various combinations of atmospheric (aerosol type and loadings) and surface (BRDF or surface spectra) conditions were paired. These parameters were used as independent and dependent variables of linear regression models to derive the coefficients of the regression models.

2.3.1.2 Sea-ice Surface Albedo
Sea-ice albedo values records the "instantaneous albedo" which is more suitable for granule albedo product. The BRDF-based direct estimation method for sea-ice surface albedo is to

develop a linear regression relationship between multispectral TOA reflectance and broadband sea-ice albedo.

$$\alpha(\theta_s) = c_0(\theta_s, \theta_v, \varphi_s) + \sum_b c_i(\theta_s, \theta_v, \varphi_s)\rho_i(\theta_s, \theta_v, \varphi_s) \tag{4}$$

where $\alpha(\theta_s)$ is the broadband blue-sky albedo; θ_s is the SZA; θ_v is the VZA; and φ_s is the RAA. i (1,2,3,4,5,7,8,10,11) represent the 9 VIIRS moderate resolution bands used in sea-ice albedo retrieval. ρ_i is the TOA reflectance from Sensor Data Records (SDRs). c_0 and c_i are the retrieval coefficients; c_0 is the constant term. The coefficients are stored in a pre-defined Look Up Table (LUT) for evenly spaced angular bins in SZA, VZA, and RAA.

The instantaneous albedo retrieved from single-date/angular observations is capable of grasping the surface dynamic change. The pre-defined LUT trained from the representative data set renders the algorithm highly efficient and accurate. The algorithm will get the coefficients for an actual $(\theta_s, \theta_v, \varphi_s)$ combination through linear interpolation in the surrounding angular bin, which runs fast in operational practices and avoids the discontinuity in neighboring albedo values. The LUT configuration covers SZA from 0° to 80° with an increment of 2°, VZA from 0° to 64° with an increment of 2°; and RAA from 0° to 180° with an increment of 5°.

The direct retrieval algorithm is designed to work over any sea-ice scenario. The strategy is to build a sea-ice BRDF database to represent different snow/ice types and various ice-seawater mixed situations. The BRDF database is the basis to derive TOA reflectance and broadband albedo respectively. This database can be retrieved from satellite data for land surface pixels but has to be simulated from physical models for sea-ice pixels due to the lack of clear and low-SZA satellite observations in polar regions.

The potential components of a sea-ice pixel include snow, ice, pond, and seawater. Then two key problems should be addressed, which are the modeling of component BRDFs and the composition into sea-ice BRDF. Here the BRDFs of snow/ice component are simulated using the asymptotic radiative transfer (ART) model, with the input of Inherent Optical Properties (IOPs) calculated from a variety of snow/ice physical parameters (Stamnes et al. 2011). For ocean water, each BRDF is a linear combination of its three components (sun glint, whitecaps, and water-leaving reflectance from just beneath the air-water interface) (Feng et al. 2016). The pond BRDF simulation in VSIA LUT deploys the analytical model proposed by Zege et al. (2015) with the optical characteristic values referred to by Morassutti et al. (1996).

Sea-ice BRDF is considered as the linear mixing of the components' BRDFs. The fractions of different components in sea-ice pixels vary through time, thus the inherent heterogeneity of sea-ice BRDF should be considered in the simulation process. The Monte Carlo simulation method is used to generate samples of fractions in assembling the sea-ice BRDF for efficiency. The fraction of the first three components is determined by a uniform random number within [0,1] and the fractions of four components sum to 1 in each BRDF item.

We generated a sea-ice BRDF dataset consisting of 120,000 simulated sea-ice BRDF items. The next key step is to generate the surface albedos. For each sea-ice BRDF item, the surface broadband albedo, including the Black Sky Albedos (BSAs) and White Sky Albedo (WSA), are derived through an angular integration and narrowband-to-broadband conversion. Another method to achieve the sea-ice albedos is by aggregating the BSAs and

WSA of each component using the simulated fractions. Its convenience embodies in the direct acquisition of snow/ice/seawater albedo from their BRDF models. The results of the two methods are consistent.

The direct estimation algorithm was to directly infer surface albedo from TOA reflectance. Another key step is to simulate the TOA reflectance and diffuse skylight factor in each angular bin from sea-ice BRDF through atmospheric simulation using the 6S (Second Simulation of the Satellite Signal in the Solar Spectrum) tool. To eliminate the uncertainty resulting from atmospheric effects, multiple possible atmospheric conditions have been considered in the training data setup. Sea ice is mainly distributed in Arctic, Southern Ocean, and Antarctic sea ice. The possible atmospheric influence in these regions can be represented in 6S using three predefined atmospheric models including Sub-Arctic Winter (SAW), Mid-Latitude Winter (MLW) and Sub-Arctic Summer (SAS), while the typical aerosol types can be described using Rural and Maritime (Vermote et al. 1997). In practice, the atmospheric parameters are pre-calculated and stored in an atmospheric LUT. We transferred the surface reflectance spectra under each atmospheric condition type, which is the combination of an aerosol model and an atmospheric model. Then the number of simulated TOA spectra is much expanded than that of the surface BRDF spectra.

For the convenience of users, our retrieval object parameter was set as blue-sky albedo, which is defined as the ratio of up-welling radiation fluxes to down-welling radiation fluxes in a given wavelength range and is comparable with the in-situ albedo observations. The blue-sky albedo is estimated using a linear relationship of black-sky albedo (directional-hemispherical surface reflectance) and the white-sky albedo (bi-hemispherical surface reflectance). The diffuse skylight factor has been recorded in the atmospheric simulation and is used to combine the BSA and WSA into blue-sky albedo (Gardner and Sharp 2010) as the regulatory factor (2).

$$\alpha_{blue-sky} = (1 - \beta)\alpha_{black-sky} + \beta\alpha_{white-sky} \qquad (5)$$

It is assumed that the BRDF dataset is representative to all possible sea-ice pixels in the polar region. Based on the calculation results above, we built linear relationships between TOA reflectance and surface blue-sky broadband albedo for different solar/viewing angular bins using a least squares method. The assumption is that the regression relationship in each angular bin is applicable to various sea-ice surface types with a minimum overall square error over the BRDF database. The regressed coefficients form the sea-ice albedo LUT.

2.3.2 Temporal Filtering

The temporal filtering algorithm is adapted from the statistical temporal filter (SFT) originally developed for the Global LAnd Surface Satellite (GLASS) albedo product (Liu et al. 2013a). SFT takes advantage of albedo climatology and temporal correlation among albedo retrievals. A linear equation is used to depict the correlation between albedo α_k on day k and albedo $\alpha_{k+\Delta k}$ on its neighboring day $k + \Delta k$:

$$\alpha_k = a_{\Delta k}\alpha_{k+\Delta k} + b_{\Delta k} + e_{\Delta k} \qquad (6)$$

where, $a_{\Delta k}$ and $b_{\Delta k}$ are regression coefficients and $e_{\Delta k}$ is the random error following Gaussian distribution with variance $\eta_{\Delta k}^2$. To obtain an estimate of albedo $\hat{\alpha}_k$ at current day k, SFT seeks to combine information from albedo retrievals $\alpha_{k+\Delta k}$ within a temporal window and albedo climatology in a statistically optimal way:

$$\hat{\alpha}_k = (\frac{\mu_k}{\sigma_k^2} + \sum_{\Delta k=-K}^{\Delta k=+K} \frac{a_{\Delta k}\alpha_{k+\Delta k}+b_{\Delta k}}{a_{\Delta k}^2\varsigma_{k+\Delta k}^2+\eta_{k+\Delta k}^2})/c$$

(7)

$$c = \frac{1}{\sigma_k^2} + \sum_{\Delta k=-K}^{\Delta k=+K} \frac{1}{a_{\Delta k}^2\varsigma_{k+\Delta k}^2+\eta_{k+\Delta k}^2}$$

(8)

where μ_k is the mean and σ_k^2 is the variance of albedo at day k from climatology, and ς^2 is the variance of albedo retrieval error.

The GLASS STF approach derives albedo climatology from Moderate Resolution Imaging Spectroradiometer (MODIS) albedo products [MCD43, Collection 5 (C5)]. For the locations covered with seasonal snow, the mean and variance of the albedo around the snow starting and ending days tend to be underestimated because the MODIS C5 albedo product typically ignores discrete snow days during ephemeral snow periods. To obtain improved snow climatology, we incorporate snow cover and albedo data from MOD10A1 data. MOD10A1 data of daily snow coverage from 2003 to 2013 are used to determine snow seasons for each pixel. For the snow-free seasons, albedo mean and variance are calculated from MCD43 albedo data. For the snow seasons, albedo climatology is derived from MOD10A and MCD43 data. The MOD10A product is used to calculate the percentage of snow-covered days and snow-free days. The albedo of snow-covered days is obtained from MOD10A1 data. The albedo mean and variance of the first day of snow-free seasons that are derived from MCD43 are used to generate samplings of snow-free background albedo for the snow-covered seasons. The generated snow-free albedo and the snow-covered albedo from MOD10A are then used to derive snow-covered climatology for the snow-covered seasons.

2.3.3 Sensitivity Analysis

2.3.3.1 Partial Cloud Coverage

The presented retrieval approach requires cloud-free VIIRS observations as input. We relied on the VIIRS cloud mask product to exclude cloud-covered pixels. The current VIIRS cloud mask data have an 8% omission error and a 4% commission error (Vermote et al. 2014). The detection of partial cloudy pixels is even more difficult because of their similar spectral signature to clear pixels. Here, we investigated the effects of undetected partial cloud coverage on accuracy of retrieving daily albedo using the simulated data. The TOA reflectance and surface fluxes of partially cloudy pixels were calculated as a combination of clear-sky simulation and cloudy-sky simulation according to the percentage of cloud

coverage. Regression coefficients to derive clear-sky daily albedo were applied to the simulated TOA reflectance to estimate daily albedo for the partially cloudy cases. The calculated daily albedo was then compared with the simulated albedo. The simulation uses a surface spectra library of 245 records covering various surface type and SZA=30° as input. Figure 2-7 shows cloud coverage led to an overestimation of daily albedo. The magnitude of positive bias and retrieval errors is dependent on the percentage of cloud coverage and cloud optical depth (COD). Even for thin clouds (COD = 5), partial cloud coverage of 20% causes a positive bias of 0.022 and an RMSE of 0.025. For thick clouds (COD = 120), a small portion (3%) of cloud within a pixel will generate an error with a similar magnitude. This sensitivity analysis stresses the importance of high-quality cloud mask products for retrieving daily albedo. Actually, the effects of undetected clouds on retrieving daily albedo are more complicated than the above simulation. Our simulation-based sensitivity analysis did not consider the diurnal dynamics of cloud coverage and properties, and it did not account for the impact of cloud shadows either.
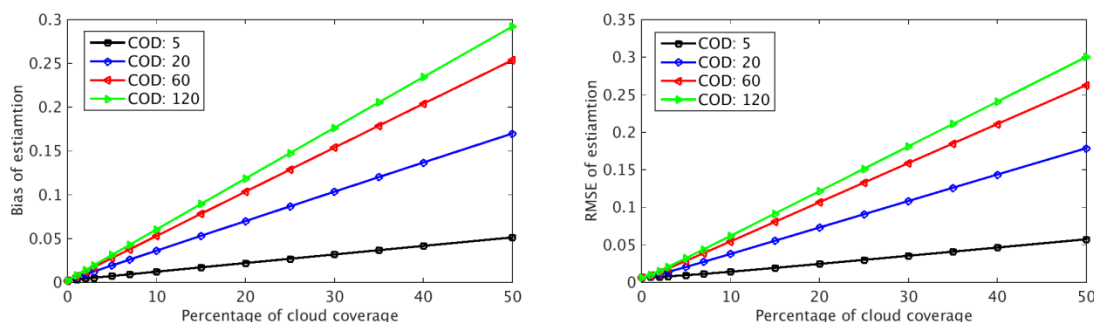
Figure 2-7. Impacts of cloud coverage on errors of retrieving daily albedo.

2.3.3.2 Aerosol Type

A single type of aerosol was typically used in previous studies of directly estimating land surface albedo (e.g., He et al. 2014; Liang 2003). Although four aerosol types were considered by Wang et al. (2013), a group of generic regression coefficients was derived in their study by combining data from all aerosol types. The authors failed to further analyze the impact of aerosol type on bias and errors in retrieving surface albedo. Here, we designed four different LUTs using training data from each of the four aerosol types. We also created a generic LUT using training data from all four aerosol types. The various LUTs were applied to simulated TOA reflectance data with different aerosol types to estimate daily albedo. The estimated results were then compared with the simulated values of daily albedo to assess errors caused by use of incorrect aerosol types (Figure 2-8). Zero bias and smaller errors occurred when the aerosol type used for the training data was the same as for the comparison data. When coefficients derived from continental aerosol were applied to the data of other aerosol types, a systematic overestimation or underestimation was produced. For biomass burning aerosol, a small positive bias (<0.01) exists. Desert aerosol has a slightly larger positive bias. For the urban aerosol type, values of daily albedo are

underestimated with a large bias >0.015. Due to the existence of a large bias in the urban aerosol results, urban aerosol cases will result in substantial retrieval errors of greater than 0.03. For all cases, a general trend of increase in bias and RMSE exists when VZA increases. The use of the generic LUT generated slightly better results than use of the continental LUT for all the aerosol types except the continental aerosol. For the continental aerosol, the retrieval quality was slightly worse, especially in terms of RMSE. We can conclude that an aerosol-specific LUT is preferred to obtain higher accuracy when accurate information about aerosol type is available. Otherwise, a generic LUT should be used instead.

a)   Continental LUT

b)   Generic LUT
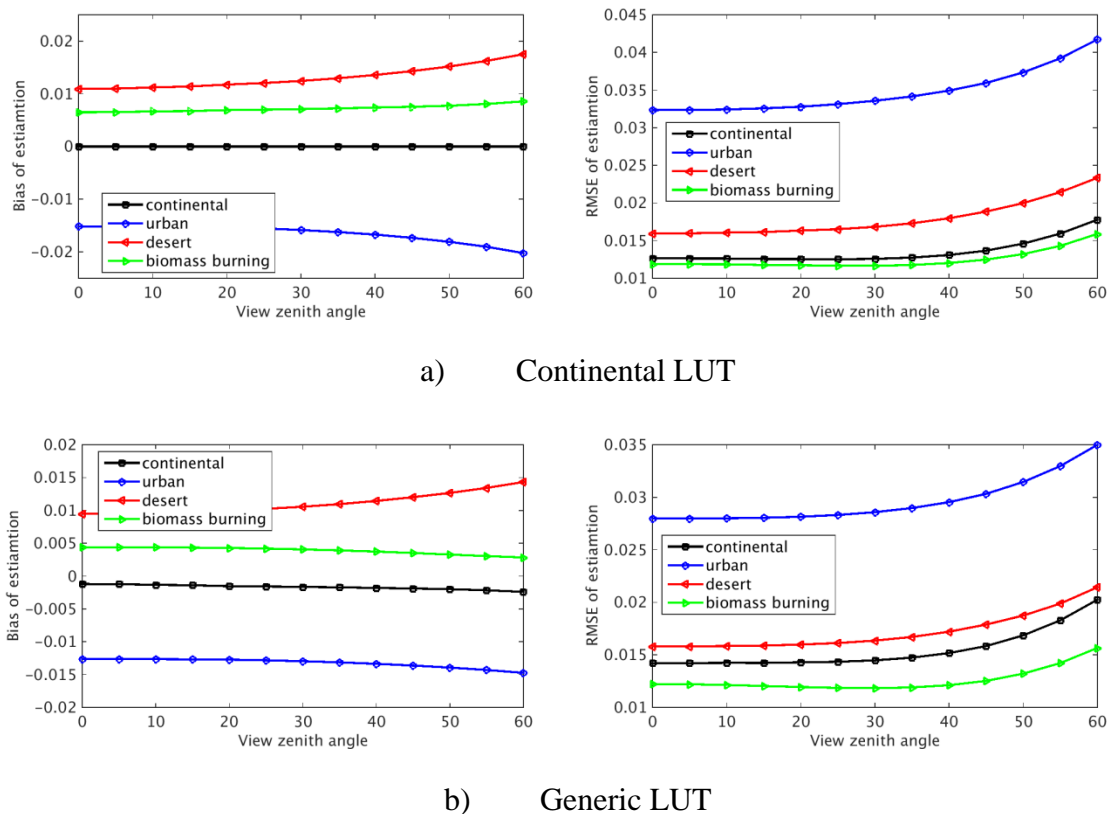
Figure 2-8. Impacts of aerosol types on errors of retrieving daily albedo.

2.3.3.3 Surface Type

Similarly, we also studied the impact of surface types on albedo retrievals, which were usually overlooked by previous studies. For example, Qu et al. (2014) categorized surface into three groups and applied surface-specific LUTs to each surface type. However, the authors did not analyze the influence of errors in information about the surface type on retrieval accuracy. In this study, a generic LUT trained with data for all surface types was applied to cases of various surface types. The generic LUT performed very well for vegetated surfaces with an ignorable bias and small RMSE (Figure 2-9). However, this generic LUT will generate substantial biases for snow and desert surfaces. Especially for desert cases, the

overestimation can be as high as 0.02. The generic LUT will underestimate daily albedo for snow cases. Although the absolute value of the bias of snow is smaller than that of desert, the RMSE of snow is much higher than that of desert. This is mainly caused by the overall greater magnitude of snow albedo. To reduce the retrieval errors for snow and desert surfaces, we developed two surface-specific LUTs. According to the sensitivity analysis of aerosol type, the desert aerosol model was used for the desert LUT. Unsurprisingly, LUTs specific to surface type generate albedo with much smaller RMSE. The reduction in RMSE is especially manifest for the desert surfaces. With the snow LUT, errors in retrieving snow albedo are still >0.02, which nevertheless represents a reduction of 0.015. These results highlight the importance of accurate information on surface type so that a surface-specific LUT can be selected.
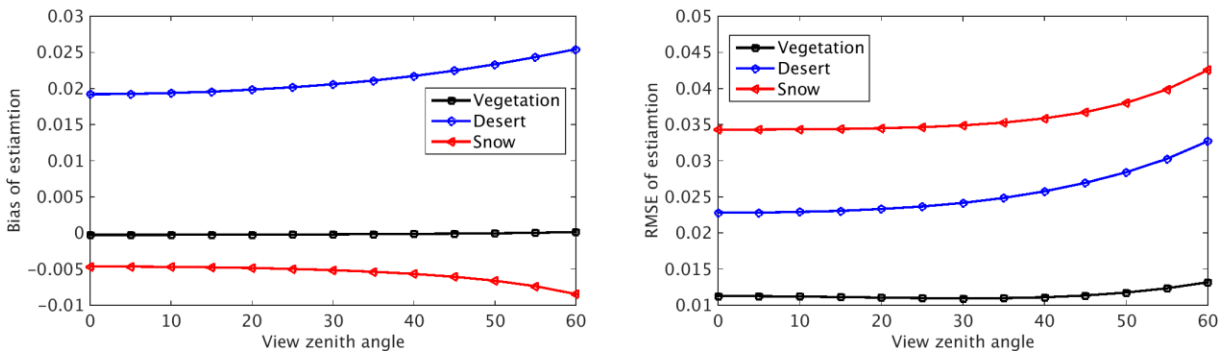
a) All surface types

b) Desert

NOAA

VIIRS Surface Albedo Algorithm Theoretical Basis Document

Page 24 of 56

c) Snow
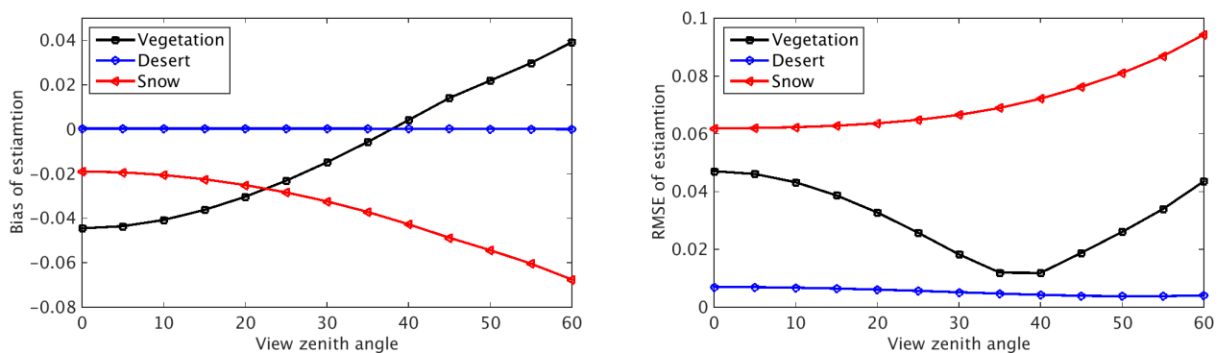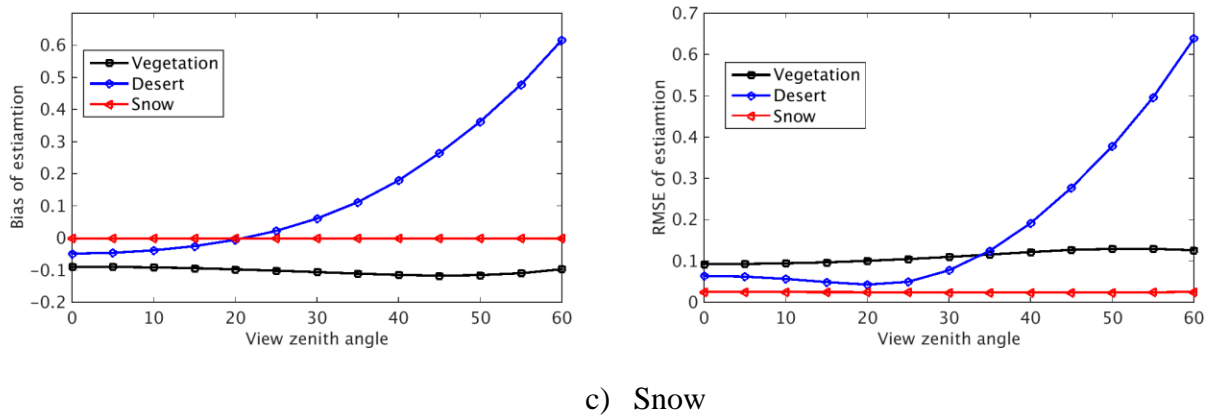
Figure 2-9. Impacts of surface types on errors of retrieving daily albedo.

2.2.3.4 Diurnal Variations of Atmospheric and Surface Conditions

To facility the computation of daily albedo, this study assumes that the atmospheric and surface conditions will not change during a day or at least that the atmospheric and surface conditions of the satellite overpass time can represent their daily variations. As a matter of fact, atmospheric parameters are dynamic, and factors such as cloud cover (Tian et al. 2004), perceptible water(Radhakrishna et al. 2015), aerosol type and loadings (Arola et al. 2013) can vary dramatically during a period of day. These factors may affect values of daily blue-sky albedo by changing magnitude and spectral distribution of downward shortwave irradiance and its diffuse portion. Similarly, surface reflectivity may also change within a period of day. For instance, events such as snow melting, soil freezing and thaw all affect surface reflectance and its directionality.

While it fails to handle the actual diurnal variations of atmospheric parameters and surface conditions, the presented method mainly considers the effects of SZA on daily albedo and shortwave radiation budget. A previous study on TOA albedo suggested that the diurnal variability of TOA albedo can be largely explained by its dependency on SZA (2014). The validation results presented here demonstrates that daily values of surface albedo can be estimated with improved accuracy after incorporating solar angle effects.

Here, we studied the effects of daily aerosol variability on albedo retrieval using the field measurements of aerosol and surface shortwave irradiance. Figure 2-10a plots a typical daily curve of aerosol optical depth (AOD) over the Bondville station. The AOD value at the equator crossing time (ECT) of VIIRS (13:30) is represented by the red dot. AOD varies from 0.037 to 0.075 for the day, and the standard deviation is as large as 0.006 (10% of mean). We simulated the daily changes of surface downward shortwave radiation using the actual daily AOD values and a constant AOD of the VIIRS ECT. The simulated results suggest such aerosol variations have little impacts on total downward shortwave radiation (Figure 2-10b) and ratio of diffuse radiation (Figure 2-10c). As a result, the daily mean albedos calculated

from the two inputs of aerosol have a relative difference smaller than 1%. However, it should be noted the sensitivity study here used limited data. Aerosol is a very dynamic factor with substantial spatial and temporal variability (Holben et al. 2001). Further study is needed to better understand the impacts of aerosol and other atmospheric or surface parameters on retrieving daily albedo.
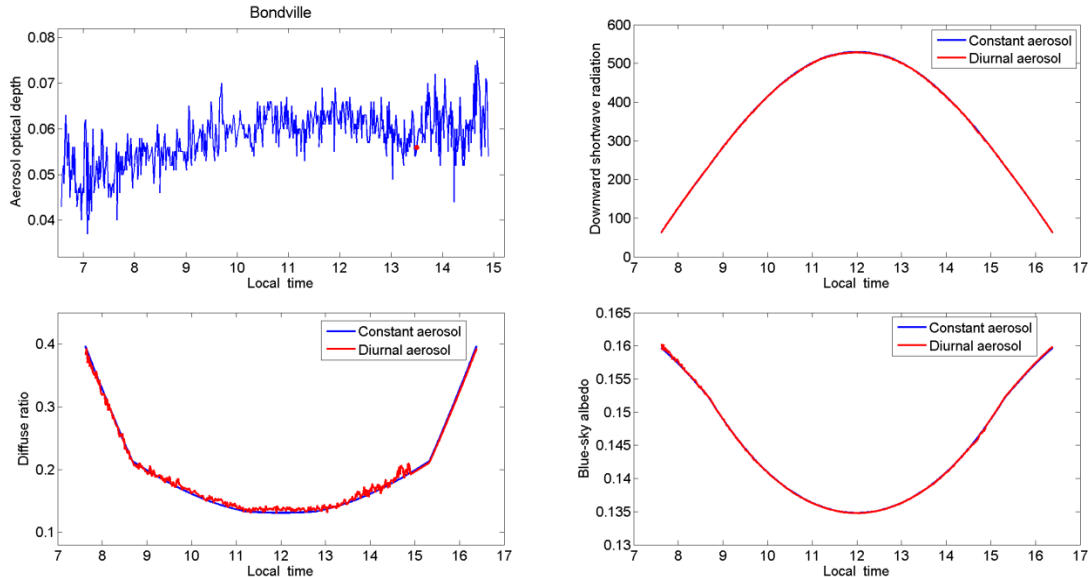
Figure 2-10. Typical diurnal variations of a) aerosol, b) downward shortwave radiation, c) diffuse ratio and d) blue-sky albedo for a typical clear day over Bondville.

2.4. Algorithm Output

The online and offline parts use different output and are described separately. The required outputs for the online processing of NDE Surface Albedo algorithm unit are listed in Table 2-3, while that of the offline processing is listed in Table 2-4.

Table 2-3. Outputs of the online processing of the NDE surface albedo algorithm unit

Output Data	Description
VIIRS_Albedo_EDR	**VIIRS Improved Surface Albedo EDR**
DataQualityFlag (DQF)	VIIRS Surface Albedo 2-bit High-level Data Quality Flag
ProductQualityInformation (PQI)	VIIRS Surface Albedo 2-byte Product Quality Information
AlbScl	VIIRS LSA Albedo Scale Factor

AlbOff	VIIRS LSA Albedo Offset
Latitude	Latitude
Longitude	Longitude
Metadata Variables	Details in metadata list in ATBD

*In the table, AlbScl, AlbOff and Metadata Variables are single values; others are data array.

Table 2-4. Outputs of the offline processing of the NDE surface albedo algorithm unit

Output Data	Description
VIIRS Filtered Surface Albedo Tiles	Gridded and temporal-filtered VIIRS Surface Albedo product. Input data for (day+2) online VIIRS Surface Albedo processing added to the historical Tile DB
Data Quality Flag (DQF)	VIIRS Surface Albedo 2-bit High-level Data Quality Flag
Product Quality Information (PQI)	VIIRS Surface Albedo 1-byte Product Quality Information

2.5. Performance Estimates

The algorithm has been tested with the actual VIIRS data as input at the global scale over various seasons. The test results have been examined and analyzed. Field measurements of surface albedo and existing satellite albedo products were used to quantitatively assess the VIIRS test results.

2.5.1. Test Data Description

Field measurements at Surface Radiation Budget Network (SURFRAD) and Greenland Climate Network (GC-Net) sites were used to validate the presented method (Table 2-5). SURFRAD has provided high-quality measurements of surface radiative fluxes since the early 1990s. Five out of seven SURFRAD stations are covered with seasonal snow and provide us with an ideal data source to assess the performance of our algorithm for ephemeral snow cases. The continuous nature of the data makes it suitable for evaluating the surface radiation budget over different seasons. The sum of the downward direct and diffuse radiation separately measured by two instruments was used as total downward radiation because it is more accurate than global downward radiation directly measured using a single pyranometer (Wang et al. 2013). Daily mean albedo was then calculated as the ratio between the sum of the daily upward shortwave radiation and the sum of the daily downward shortwave radiation. Daily values were generated only for days when half of the daytime measurements are valid.

The MODIS albedo product has been extensively validated over a wide range of land cover types by numerous independent investigations (e.g., Cescatti et al. 2012). Two versions of MODIS albedo data will be used in this study: Collection 5 (C5) and Collection 6 (C6). The MODIS C5 and earlier algorithms use MODIS surface reflectance within a 16-day window as input to fit a kernel-driven bidirectional reflectance distribution function (BRDF) model (Schaaf et al. 2002). The C5 algorithm cannot accurately estimate albedo for ephemeral snow events because of the rapidly changing surface reflectance during such events. The MODIS C5 albedo product is generated every 8 days. The MODIS C6 algorithm produces daily albedo estimates and enhances its capability in handling unstable surfaces by emphasizing the contributions of observations from the current day and separating snow-covered observations and snow-free observations within the composite window. In this study, we used C5 and C6 versions of MCD43A1 BRDF data. Daily mean blue-sky albedo was calculated from the MODIS BRDF parameters and MODIS aerosol product with consideration of daily changes in SZA. Many previous validation studies have focused on MODIS albedo retrievals over snow-free or stable snow surfaces. The capability of predicting a gap-free albedo field, particularly for ephemeral snow events, is typically overlooked. In this study, we will compare gap-filled VIIRS and MODIS data and assess their application in studying surface radiation budget.

Table 2-5. List of field measurement stations used for validating VIIRS albedo retrievals.

Site	Latitude	Longitude	Surface type	Network
Fort Peck, MT	48.31	-105.10	Grassland	SURFRAD
Bondville, IL	40.05	-88.37	Agriculture	SURFRAD
Goodwin Creek, MS	34.25	-89.87	Forest/Pasture	SURFRAD
Penn State, PA	40.72	-77.93	Cropland	SURFRAD
Sioux Falls, SD	43.73	-96.62	Grassland	SURFRAD
Boulder, CO	40.13	-105.24	Grassland	SURFRAD
Desert Rock, NV	36.63	-116.02	Desert	SURFRAD
GITS	77.14	-61.04	Snow	GC-Net
Humboldt	78.53	-56.83	Snow	GC-Net
Summit	72.58	-38.51	Snow	GC-Net
DYE-2	66.48	-46.28	Snow	GC-Net
Saddle	66.00	-44.50	Snow	GC-Net
South Dome	63.15	-44.82	Snow	GC-Net
NASA-SE	66.48	-42.50	Snow	GC-Net
NEEM	77.50	-50.87	Snow	GC-Net

GLASS albedo is a long-term global product of surface albedo, which has been available from 1981 to the present (Liang et al. 2013; Liu et al. 2013b). MODIS data have been the main data source used to generate the product from 2000 (Qu et al. 2014), and AVHRR was used before the MODIS era. In addition to land surface albedo, the GLASS albedo Phase-2 product includes albedo values over ocean and sea-ice surfaces (Qu et al. 2016). The

GLASS land surface albedo algorithm is also a direct estimation method. Albedo is initially retrieved from each clear-sky satellite observation. Albedo retrievals from a rolling window of 16 days are then averaged to generate an intermediate albedo product at an interval of 8 days. A statistical temporal filter (SFT) is applied to the intermediate product to fill data gaps caused by persistent cloud coverage and to reduce retrieval noise (Liu et al. 2013a). GLASS albedo V04, the latest version, was used in this study. GLASS albedo values are black-sky and white-sky instantaneous albedo corresponding to local noon time. The difference between local noon albedo and daily mean albedo will be ignored when we compare GLASS albedo with VIIRS albedo.

2.5.2. Results Analysis

Figure 2-11 shows the global maps of VIIRS land surface albedo on July 17, 2015, obtained using the direct retrieval and temporal filtering processes. The granule files obtained from the direct retrieval process were gridded for illustration and comparison. Due to cloud coverage, the VIIRS direct retrieval results contain numerous missing values. In addition, there are no valid retrievals over the entire Antarctica because of the absence of solar radiation during the polar night. The granule-based data structure and missing values make it difficult to directly use the granule data products. The temporal filtering process generates a continuous map over all land pixels. Even over the polar night area of Antarctica, pixels are filled with climatological information. For comparison, the MODIS map of daily mean albedo is also generated from the MODIS C6 BRDF product. Although the VIIRS and MODIS maps show similar spatial patterns, it should be noted that the MODIS map still contains filling values even though the data from a 16-day window are used. Gaps in the MODIS data are particularly prominent at the Intertropical Convergence Zone (ITCZ) and the Asian monsoon area where clear-sky observations are limited.
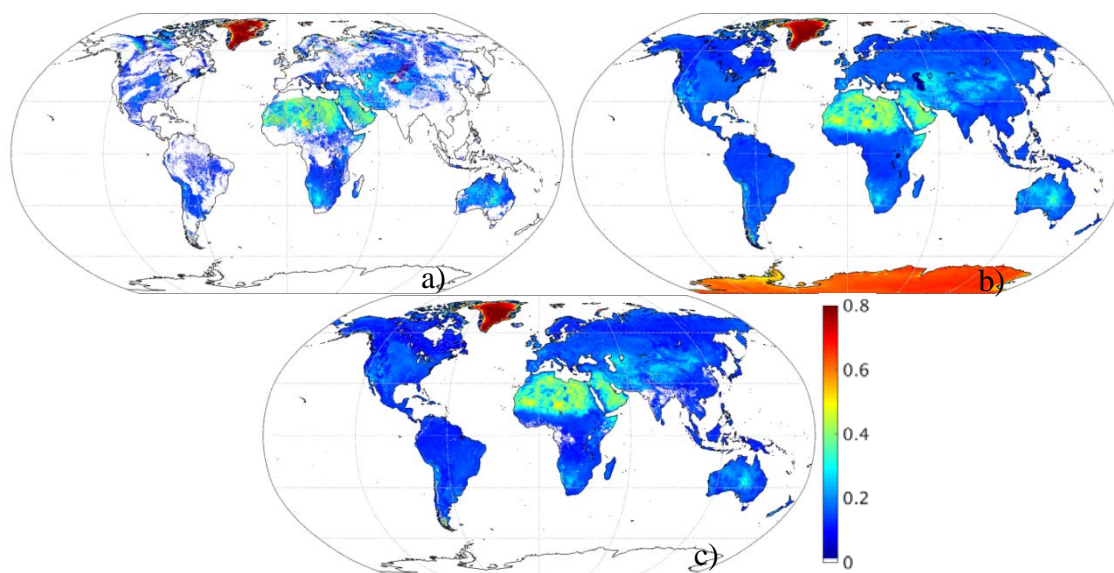
Figure 2-11. Global maps of VIIRS land surface albedo on Jul 17, 2015, produced by direct retrieval (a) and after temporal filtering (b). A map of the MODIS C6 albedo product (c) is also shown for comparison.

2.5.2.1 Validating Land Surface Albedo

Snow-free Results

All valid clear-sky retrievals of daily albedo were compared with corresponding SURFRAD measurements (Figure 2-12). The two datasets generally show good agreement with an R2 of 0.839, a negligible underestimation, and an overall RMSE of 0.056. The accuracy is comparable to previous results for retrieving instantaneous albedo (Wang et al. 2013). Compared to the data retrieved with BRDF LUT, the results for Lambertian LUT are slightly worse. Together with the following results for the GC-Net stations, we will discuss the pros and cons of incorporating surface anisotropy in estimating daily albedo. For both BRDF and Lambertian results, larger discrepancies are mainly observed for the snow-covered cases. Due to a mixture of snow and vegetation, even the relatively homogenous SURFRAD sites will have less spatial representativeness for snow-covered albedo. To reduce errors caused by partial snow coverage, we used the data for permanent snow cover from GC-Net stations to assess the quality of snow albedo retrievals.

Figure 2-12. Comparison results between VIIRS-retrieved daily albedo and that measured at SURFRAD sites. All available data are used.

The direct estimation method uses one single observation to retrieve daily albedo. In nature, such retrievals will reflect internal and external effects such as intra-daily variations due to subpixel clouds and shadows as well as differences in atmospheric conditions and viewing geometry. To reduce the impacts of these factors, we calculated 16-day averaged values of daily albedo and compared them with field measurements for snow-free days (day of year 121–272, Figure 2-13). The 16-day averaged retrievals generally show improved quality. The RMSE from BRDF LUT is as small as 0.018. This accuracy is even higher than what we

previously obtained for instantaneous albedo (Wang et al. 2013), mainly due to the use of aerosol-specific LUT for the desert cases.
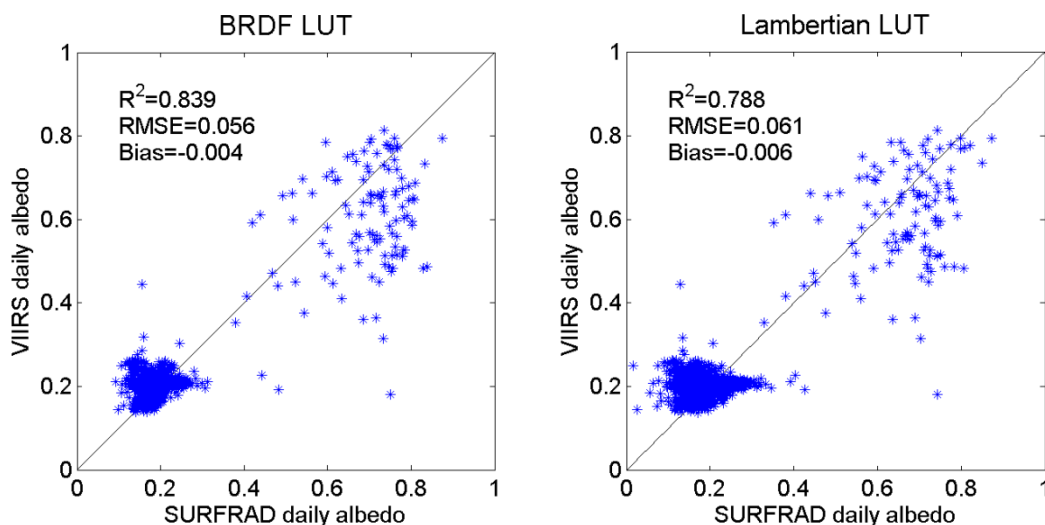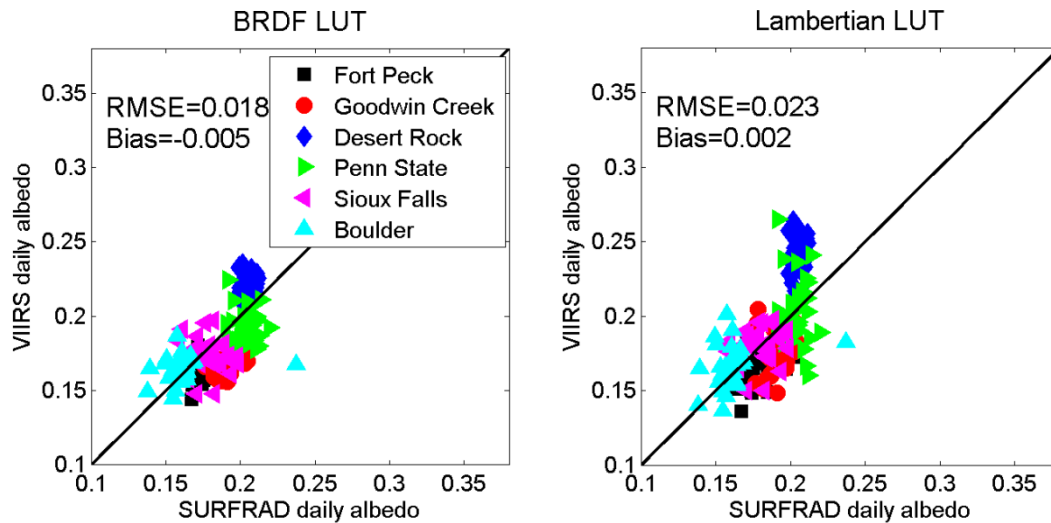

Figure 2-13. Comparison results between VIIRS-retrieved daily albedo and that measured at SURFRAD sites. Only snow-free data are used.

2.5.2.2 Snow-covered Results

Uncertainties of snow albedo are generally larger, especially for cases with long oblique view path or large SZA values. Scatterplots of snow albedo retrievals were made by excluding far off-nadir observations (SZA >55° or VZA >30°) with three different LUTs (Figure 2-14). It is interesting to note that the Lambertian LUT generates the best results with the smallest RMSE. Correlations between retrieved daily albedo and measured daily albedo are similar amongst the three LUTs, and the generic BRDF LUT has a slightly higher R^2. However, due to the existence of a non-identity slope, the generic BRDF LUT underestimates daily mean albedo with the largest bias of 0.047. The snow-specific BRDF LUT reduces the bias, but the non-identity slope still exists. It implies that BRDF information used in training the models has uncertainties and is not able to sufficiently duplicate the actual angular distribution of snow reflectance. With such inaccurate information about snow BRDF, the BRDF version of LUT fails to outperform the model with the Lambertian assumption. The Lambertian LUT was trained with surface spectra where complete information about surface spectral reflectance was available and nine VIIRS bands were used to derive the model. The BRDF LUT obtains the spectral BRDF information from the MODIS BRDF database. To reduce the correlation among bands, only one of the three blue bands were used in the BRDF model construction (Wang et al. 2013). In addition, the broadband albedo of the BRDF data was empirically converted from the narrowband albedo and the narrow-to-broadband conversion may have caused additional uncertainties.
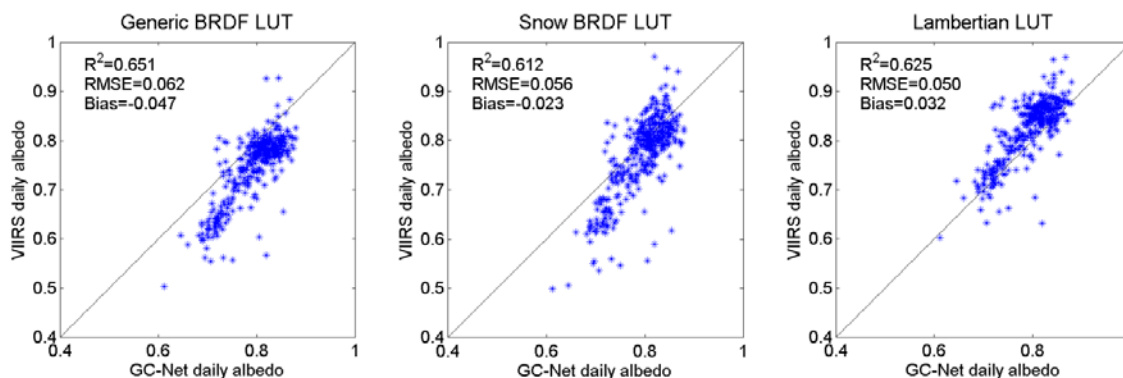
Figure 2-14. Comparison results between VIIRS-retrieved daily albedo and that measured at GC-Net sites. Data shown here are limited to SZA<55° and VZA<30°.

Ideally, a database of full spectrum BRDF is the best candidate to train the model. However, data availability determines the tradeoff between spectral and angular information. The optimal choice is dependent on many factors such as the anisotropy of the surface reflectance, the reliability of spectral BRDF information, and the uncertainties in narrow-to-broadband conversion. Results shown in Figure 2-13 clearly suggest that BRDF information will generate less scattering, smaller errors, and higher accuracy for non-snow surfaces. Data from spectral BRDF rather than surface spectra should be used in model construction for snow-free cases. On the other hand, results for snow-covered surfaces (Figure 2-14) demonstrate that surface spectra may result in higher accuracy than spectral BRDF, at least when BRDF information contains a large degree of uncertainty.

Results for retrievals from SURFRAD and GC-Net stations were combined to evaluate the overall quality of daily mean albedo (Figure 2-15). The results for GC-Net surfaces are based on the Lambertian LUT and limited to near-nadir observations (SZA >55° and VZA >30°). The overall accuracy of retrieving daily albedo has a bias of 0.003 and RMSE of 0.055. Large discrepancies exist over snow cases, particularly seasonal snow at the SURFRAD stations. In addition to the complexity of snow albedo, which will be discussed in the following section, the use of a single observation in retrieving daily albedo will also lead to some level of random errors. After excluding the seasonal snow results from the SURFRAD stations, the validation results of 16-day mean albedo are improved to R2 of 0.996 and RMSE of 0.024 (Figure 2-16).
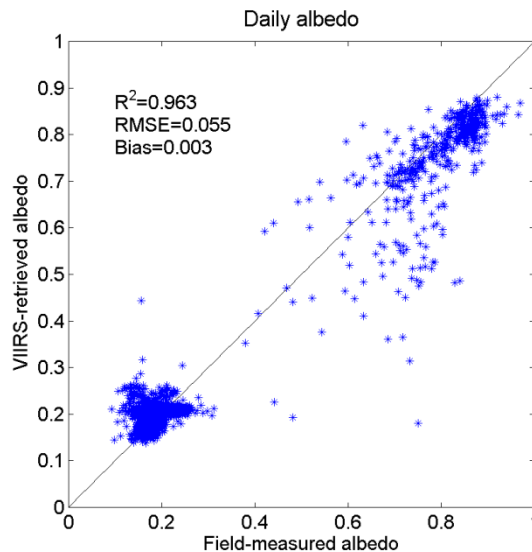
Figure 2-15. Validation results of VIIRS-retrieved daily albedo by combing data from SURFRAD and GC-Net stations. GC-Net data are limited to SZA<55° and VZA<30°.
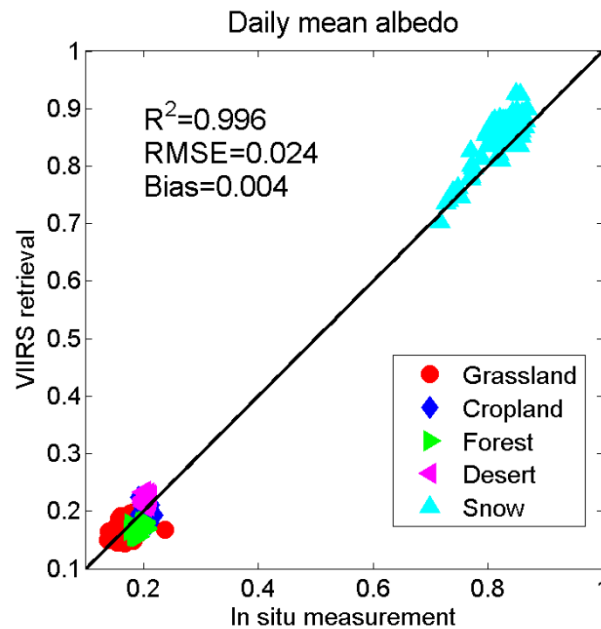
Figure 2-16. Validation results of 16-day averaged daily albedo. Snow-free albedo retrieved with BRDF LUT and snow albedo from Lambertian LUT.

Assessing Effects of Temporal Filtering

We also quantitatively compared the VIIRS daily mean albedo product before and after temporal filtering with the daily mean albedo calculated from the MODIS C6 BRDF product

(Figure 2-17). Although these products are generated from different satellite data and based on different retrieval algorithms, the VIIRS albedo data after temporal filtering are remarkably consistent with the MODIS albedo data, with a coefficient of determination of 0.94, bias of 0.013, and an RMSE of 0.035. The comparison between the VIIRS albedo before filtering and the MODIS data displays considerably greater scattering. The larger discrepancies are mainly attributable to two factors: (1) the VIIRS albedo before filtering is retrieved from a single observation and contains some random noise; (2) the original VIIRS albedo suffers from the contamination of undetected clouds, and this phenomenon is prominent around MODIS albedo values of 0.1 where the VIIRS albedo has a rather dynamic range. The substantial improvement obtained following temporal filtering indicates that the temporal filtering procedure not only fills data gaps but also improves albedo estimates over pixels with valid retrievals.
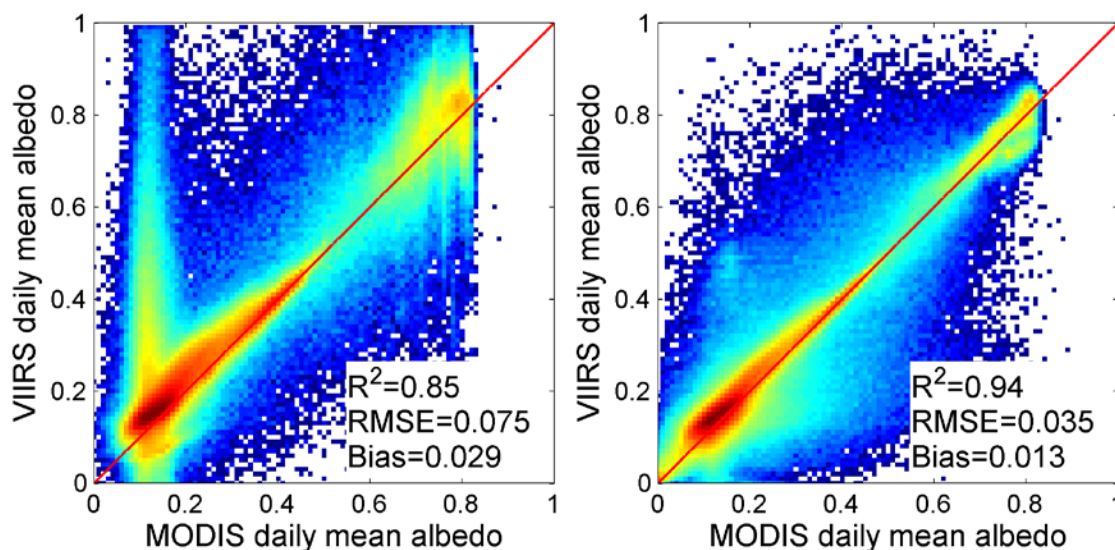
Figure 2-17. Comparison of the VIIRS albedo produced by direct retrieval (left) and after temporal filtering (right) with the MODIS albedo data.

The effects of the statistical temporal filter in filling data gaps and reducing retrieval errors can be better illustrated by an example of time series data. Figure 2-18 shows VIIRS albedo in 2013 over Fort Peck before and after temporal filtering. The albedo data from MODIS and field measurements are also displayed for comparison. Fort Peck with a latitude of 48.31°N is typical of sites covered with seasonal snow. All the four albedo values estimated from VIIRS or MODIS data are relatively consistent with values for snow-free dark surfaces. However, only the VIIRS data after temporal filtering can provide a gap-free continuous time series. The filtered VIIRS data agree well with field measurements, capturing most of the major snowfall and snow melting events. The temporal filter filled the data gaps resulting from cloud coverage and also reduced the fluctuations in albedo retrievals for stable surfaces during the snow-free growing seasons. However, we also noticed that the temporally filtered VIIRS results are dependent on the frequency and quality of clear-sky albedo input from the

direct retrieval process. For the last 30 days of the year, the site was continuously covered with clouds and there were few clear-sky observations available. Neither C5 nor C6 versions of MODIS albedo products have valid retrievals for this period. The temporally filtered VIIRS estimates also suffered from issues of large uncertainties because of the spurious retrieval of Day 355 from the direct retrieval process.
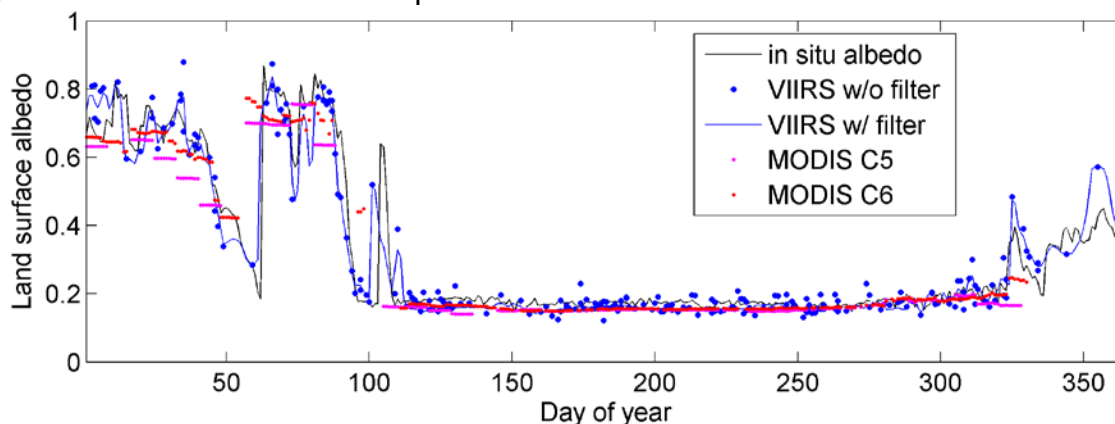
Figure 2-18. Land surface albedo for the year 2013 at Fort Peck obtained from field measurements, VIIRS direct retrieval and temporal filtering, and MODIS C5 and C6 products.

To quantify the effects of the statistical temporal filter on albedo estimates, we evaluated the VIIRS albedo results before and after temporal filtering for clear-sky days that have valid VIIRS albedo directly retrieved (Figure 2-19). The improvement over the snow-covered cases is marginal. A slight reduction in bias was observed, and the RMSE decreased by only 0.003 (<2%). It is easy to understand that climatology and neighboring observations make limited contributions because surface albedo changes dramatically from day to day for ephemeral snow events. There was, however, a notable improvement over stable surfaces. The RMSE of snow-free albedo is reduced by 13% from 0.039 to 0.034 after temporal filtering. The surface albedo in non-snow seasons is relatively stable and incorporation of historical and neighboring observations reduces random errors resulting from the use of single observations.
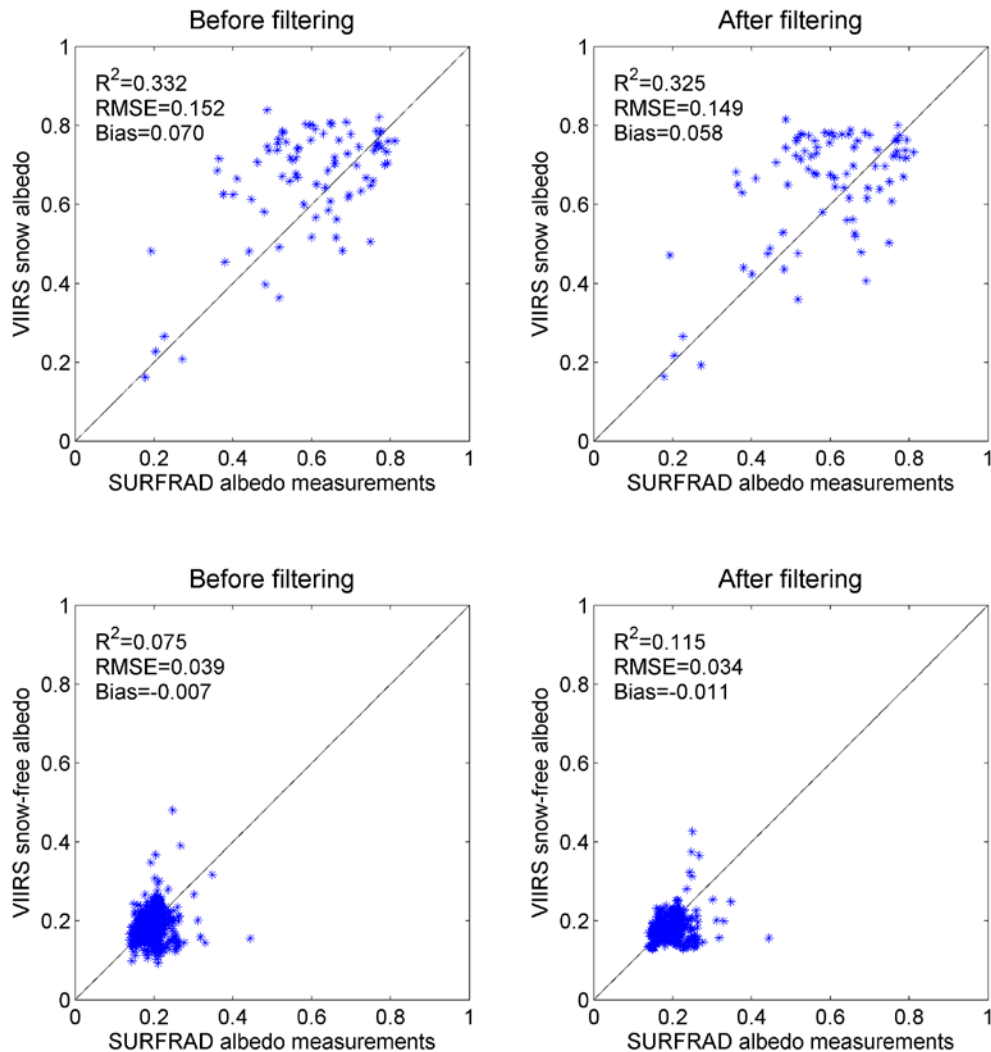
Figure 2-19. Validation results of VIIRS albedo for clear-sky days from the direct retrieval and temporal filtering processes.

To evaluate the overall quality of temporally filtered VIIRS albedo data, the gap-filled VIIRS daily albedo retrievals for all-sky conditions were compared with field measurements at all the stations (Figure 2-20). The red circles in Figure 5 represent the results for clear-sky days with valid VIIRS direct retrievals. The black text summarizes the statistics obtained by assessing all data and the red text represents the statistics for clear-sky data only. The results for days with clear-sky observations are comparable with those obtained using existing products, with an RMSE of 0.062 and a slight negative bias of -0.003. The filled data for

cloudy-sky during snow seasons still contain large uncertainties, which result in a degradation of overall statistics. At the daily temporal scale, the RMSE for all-sky data is 0.094. It should be noted that the large errors are mainly caused by cloudy-sky days during ephemeral snow events, when surface albedo varies substantially from day to day. Under such circumstances, there is a large variance in albedo values estimated from neighboring retrievals and climatology.
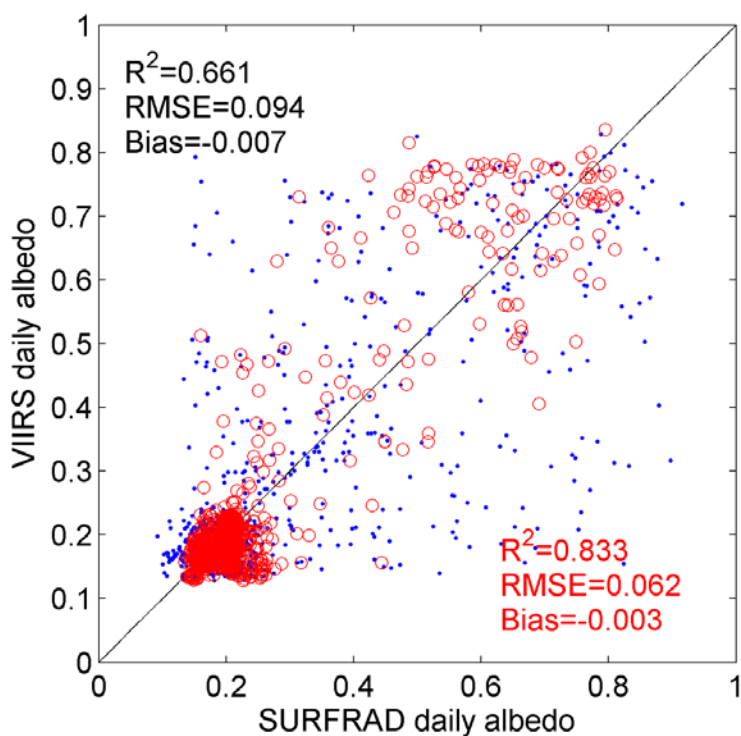
Figure 2-20. Validation of the temporally filtered VIIRS daily albedo for clear-sky and cloudy-sky days. Data of clear-sky days with valid temporally filtered VIIRS albedo are marked by red circles.

Fortunately, the uncertainties of temporally aggregated albedo data will be significantly smaller. Figure 2-21 compares the temporally filtered VIIRS albedo data averaged over 16-day windows at 8-day intervals, which is similar to the temporal composite strategy of the MODIS C5 and GLASS albedo algorithms. For the 16-day mean VIIRS results after temporal filtering, RMSE is reduced to 0.059. The correlation with field data is also improved and R2 increases to 0.793. The validation results of the 16-day mean albedo calculated from MODIS and GLASS products are also shown. To make a valid comparison, gaps in the MODIS and GLASS results were also filled using a linear interpolation approach. The MODIS C5 albedo results tend to underestimate the albedo of ephemeral snow cases because one set of BRDF kernel parameters is retrieved for a 16-day window. The improved C6 algorithm, which

emphasizes the contributions of observations from the current day and takes into account changes in snow cover during the 16-day composite window, shows substantial improvement and generates results with higher R2 and smaller RMSE and bias. The GLASS albedo has an R2 value of 0.693, RMSE of 0.076, and bias of -0.036. The underestimation of GLASS albedo can be partially attributed to the use of the local noon albedo in comparisons because the GLASS product does not contain daily mean values, nor does it provide BRDF parameters that allow us to calculate the mean. The GLASS results are inferior to those of MODIS C6 but superior to those of MODIS C5. Nevertheless, our comparison suggests that the VIIRS results after temporal filtering have the highest quality.
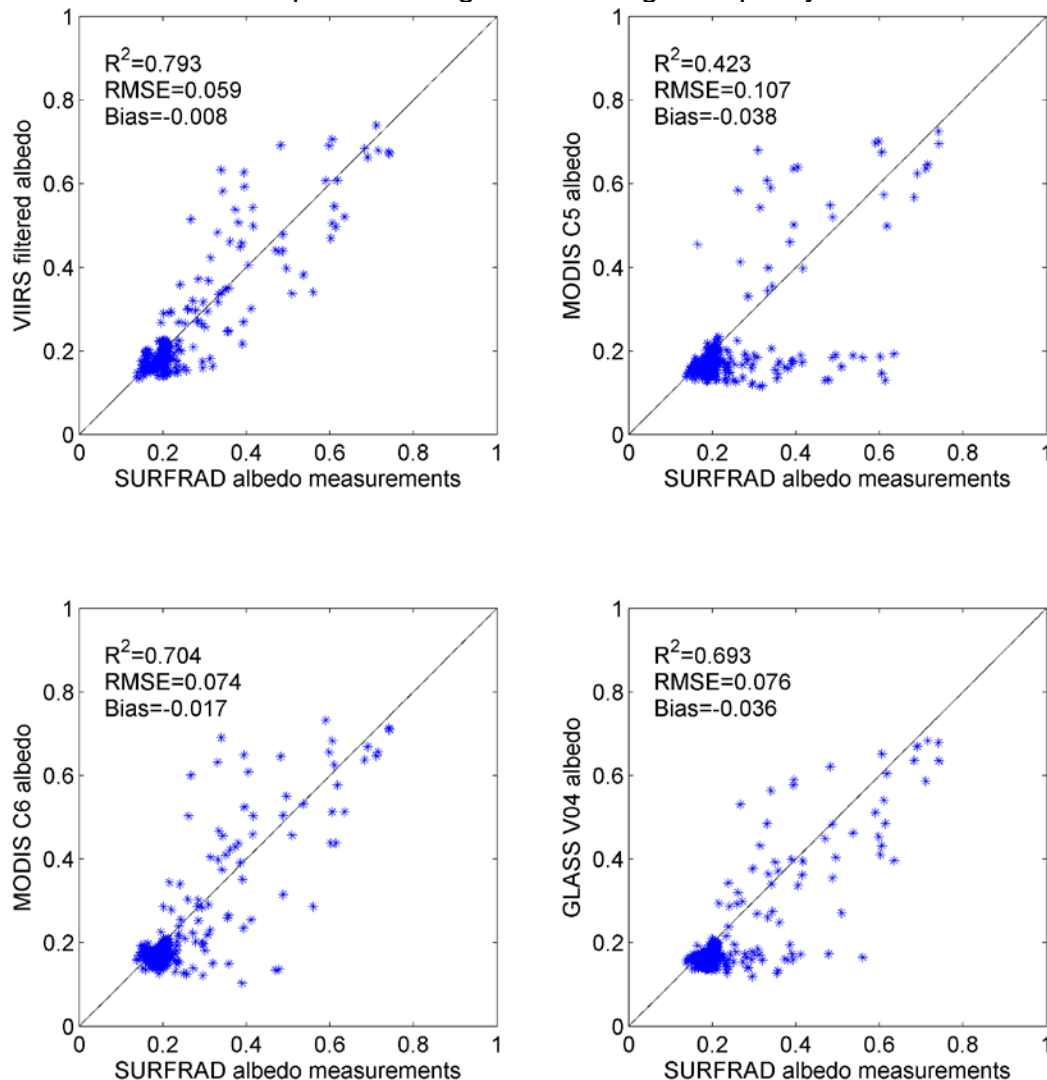
Figure 2-21. Comparison of the16-day mean albedo from VIIRS albedo data after temporal filtering, gap-filled MODIS C5 and C6 data, and GLASS albedo data.

To better compare with MODIS albedo products, we also use MODIS quality control (QC) information to select only the high-quality MODIS albedo data. For MODIS C5 data, the "BRDF_Albedo_Quality" of the MCD43A2 file corresponding to each MCD43A1 file is used and only good-quality data are used (Figure 2-22). The MODIS results from the high-quality retrievals are greatly improved compared with those shown in Figure 2-21. All MODIS data were used and missing data were interpolated to provide continuity in Figure 6. The RMSE was reduced by more than 50% from 0.107 to 0.049. The results indicate that by applying QC, we can improve product performance, albeit with a significantly reduced availability of valid products. Even after applying the QC information, there remain cases with large uncertainties, which are caused by the unstable surface conditions that occur during snow seasons. This indicates that the single-bit information of BRDF_Albedo_Quality cannot exclude all the data with low quality. For MODIS C6 data, the "Mandatory_Quality_shortwave" of the MCD43A1 file is used and only good-quality data are used for comparison (Figure 2-23). The results were limited to snow-free cases because good-quality data is required. The RMSE values of both the VIIRS and MODIS results were accordingly markedly reduced. The VIIRS results are slightly better than those of MODIS, with a 10% smaller RMSE. It is interesting that both results have one case of substantial underestimation, where SUFRAD shows a high value of snow albedo. This data point represents the data of day 363 at Boulder. Given the heterogeneity of the site, the underestimate can probably be attributed to the scaling effects of snow cover.
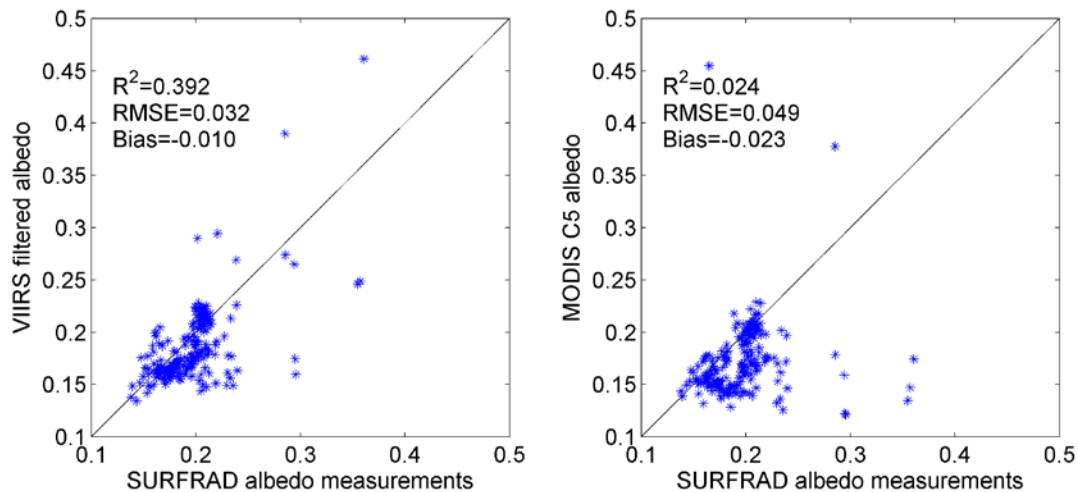
Figure 2-22. Comparison of the 16-day mean albedo from temporally filtered VIIRS data and high-quality MODIS C5 data.
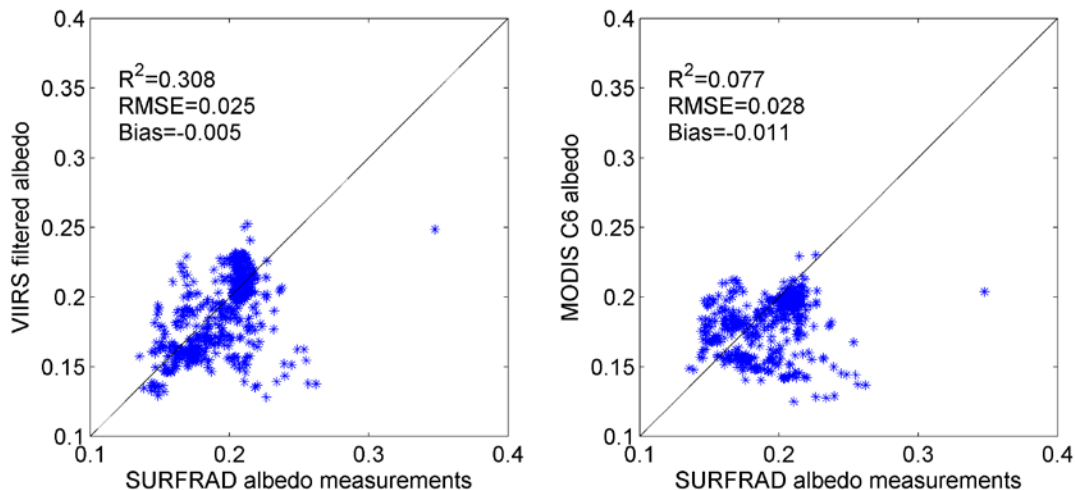
Figure 2-23. Comparison of the daily albedo from temporally filtered VIIRS data and high-quality MODIS C6 data.

2.5.2.2 Validating Sea-ice Surface Albedo

The GC-Net ground shortwave albedo values were calculated from the ratio of upwelling to downwelling shortwave radiation measurements. Considering the diurnal variation of surface albedo due to SZA and atmospheric conditions, we narrowed the comparison on the data collected at local noon from 11:30 am to 12:30 pm (13:30 pm to 14:30 pm in UTC). The VIIRS sea-ice albedo represents the instantaneous clear-sky-albedo of earth surface. Thus the satellite retrievals can be directly compared with the in situ measurements. Only clear sky observations account for the accuracy assessment.

More than five years of VIIRS and the GC-Net station data over Greenland area have been processed and compared to the calculated albedo results. Figure 2-24 shows the scatterplot between clear-sky-albedo calculated from GC-Net and surface measurements using the available data since January 2012.
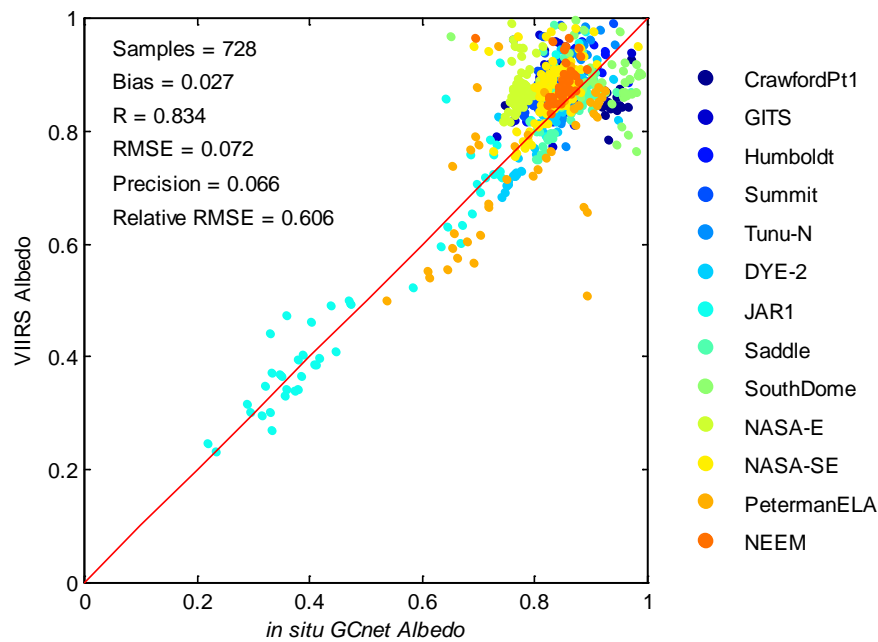
Figure 2-24. Scatter plots of Albedos derived from VIIRS sea-ice LUT vs. Albedos estimated from GC-Net stations. Datasets are stratified for each site. Different colors are used for marking the data pairs of different sites.

There are three data pairs, apparently below the 1:1 line, that demonstrates an underestimation of VIIRS albedo product. We found all of them are collected from an identical site (PetermanELA) on neighboring days. Figure 2-25 shows the surrounding albedo maps and the dates, in which the center pixel covers the site position. It is shown that there is an apparent albedo contrast close to the site which causes apparent heterogeneity. Therefore, the high discrepancy at these data pairs is possibly caused by the surface heterogeneity and geometric error (Baker et al., 2011; Peng et al., 2015).
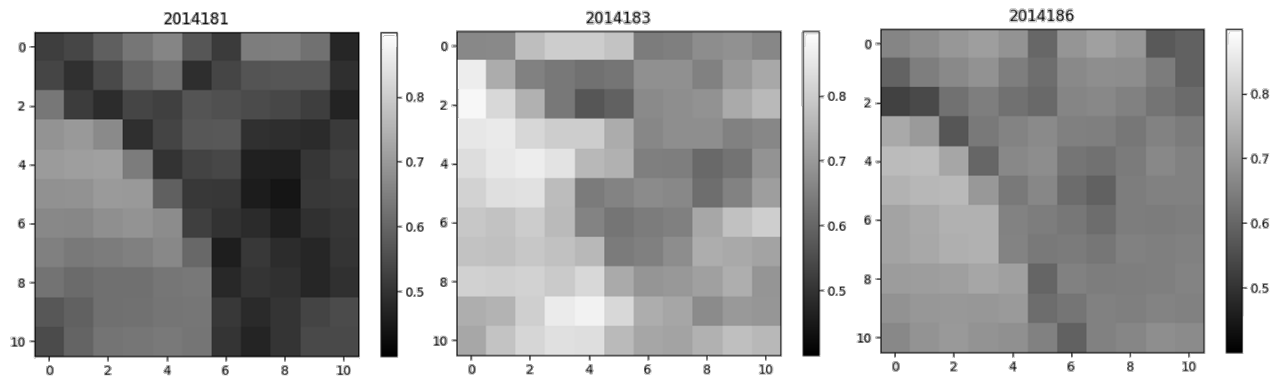
Figure 2-25. VIIRS albedo map around the PetermanELA site. The gray color illustrates the albedo value.

For each GC-Net site, overall accuracy, precision, and uncertainty are estimated by calculating the mean albedo difference, the standard deviation of VIIRS estimated albedo and the RMSE (Root Mean Square Error) between VIIRS albedo and GC-Net albedo. The calculation results are summarized in Table 2-6.

Table 2-6. Validation results at each GC-Net station

Site No.	Site Name	No. of match-up	Bias	RMSE
2[*]	CrawfordPt1	25	-0.0571	0.0907
4[*]	GITS	43	0.0661	0.0796
5	Humboldt	53	0.023	0.0409
6[*]	Summit	71	0.0732	0.0798
7	Tunu-N	47	0.0131	0.0382
8[*]	DYE-2	61	-0.0062	0.0363
9	JAR1	55	0.0186	0.0605
10[*]	Saddle	58	-0.0072	0.0474
11[*·]	SouthDome	42	-0.0327	0.0989
12[*]	NASA-E	78	0.0998	0.1066
15	NASA-SE	97	0.041	0.0636
22[*·]	PetermanELA	46	-0.0353	0.1052
23	NEEM	52	0.0395	0.0583

It is seen that the exact accuracy and precision values are different from site to site. Nevertheless, the absolute value of overall accuracy is 0.027 with a precision of 0.066, while the precision of GC-Net observations is around 0.05 (Steffen et al.,1996). The result indicates that the sea-ice LUT is efficient to retrieve the albedo of ice/snow surface. The overall Root Mean Square Error is 0.072 for all sites, which reflects the spread of the retrieved albedo.

The hypothesis test was conducted at 5% significance level. (1) Assuming the match-ups represent the accuracy of the VIIRS sea-ice albedo, the acceptance interval of the VIIRS sea-ice albedo bias is (0.023, 0.031) from a t-test. (2) The site-specific hypothesis test on bias demonstrates the existence of local bias at some sites (marked with "*" in Table 2). (3) Meanwhile, the site-specific hypothesis test on the variance of the error shows only two sites (marked with "·" in Table 2) has significant different precision from the whole sample. The other sites have the statistically constant precision of 0.066. The local bias and precision are relevant to the surround heterogeneity and in situ measurement quality at each site.

Due to the high latitude of the Greenland region, the SZA corresponding to the observations are distributed from 40° to 82° peaked at around 50°~55°. The bias between VIIRS albedo and GC-Net observations slightly increases with SZA shown in Figure 2-26.
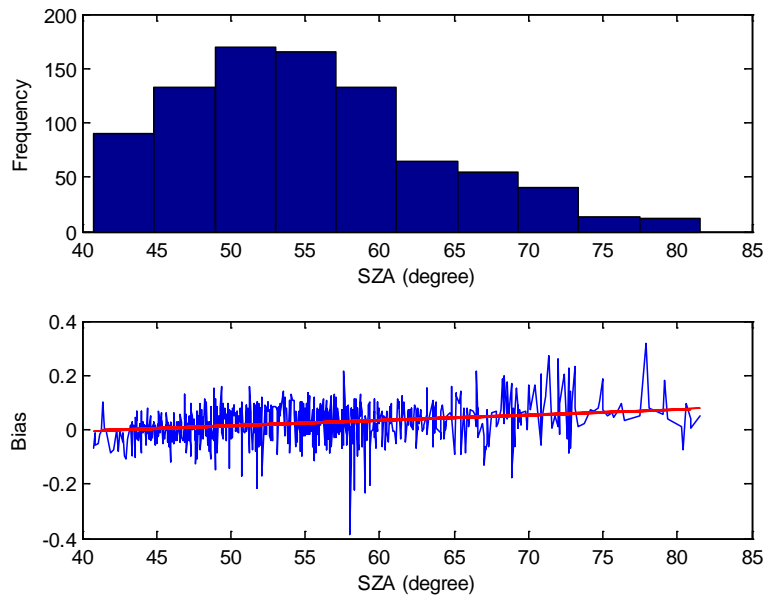
Figure 2-26. The distribution of SZAs of the data pairs (up) and Variation of Albedo discrepancy along with SZA.

2.6. Practical Considerations

2.6.1 Numerical Computation Considerations

Accurate retrieval of albedo requires reliable acquisition of atmospheric parameters. Forward running of atmospheric radiative transfer model is time-consuming and not suitable for operational retrieval of albedo. Instead, the LSA algorithm pre-runs the atmospheric radiative transfer at some given conditions and stores the parameters into the LUTs to save computational time.

2.6.2 Programming and Procedural Considerations

The LSA algorithm includes two major steps: direct retrieval and temporal filtering. The temporal filter part needs time series of historical LSA retrievals as input. The direct retrieval procedure is granule-driven and executed for each daytime granule. The temporal filtering process is tile-driven and executed at the end of each day.

2.6.3 Quality Assessment and Diagnostics

2.6.3.1 Quality flag

There are two quality flag arrays available with the EDR product. In which, Product Quality Information (PQI) flags are provided for the data quality information, and Data Quality Flag (DQF) flag is provided for the product monitoring purpose.

(a) Product Quality Information flags

Bit Position   7 6 5 4 3 2 1 0   7 6 5 4 3 2 1 0

Byte 1   Byte 0
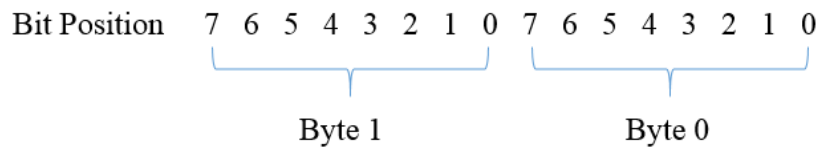
Table 2-7. Product Quality Information (PQI)

Byte	Bit	Flag	Source	Description
0	0-1	Overall quality	LSA	00: high-quality retrieval, 01: retrieval, 10:no retrieval
	2-3	Cloud condition	Cloud mask	00=confidently clear, 01=probably clear,10=probably cloudy,11=confidently cloudy
	4	SDR quality	SDR	0 = normal , 1 = bad data
	5	Solar zenith angle flag	SDR	0: favorable SZA, 1: very large SZA (>60)
	6	View zenith angle flag	SDR	0: favorable VZA, 1: very large VZA (>60)
	7	Spare		
1	0-2	Retrieval Path	LSA	000: generic, 001: desert, 010: snow, 011: sea-ice, 100: no retrieval
	3-4	Temporal filter quality flag	LSA	00: high-quality retrieval, 01: degraded retrieval, 10:no retrieval
	5	Online filter flag	Online filter	0: no filter, 1: filtered
	6-7	Spare		

(b) Data Quality Flag

Bit Position   7 6 5 4 3 2 1 0

Byte	Bit	Flag	Source	Description

0	0-1	Overall quality	LSA	00: high-quality retrieval, 01: retrieval, 10:no retrieval

Table 2-8. Quality flag for offline VIIRS albedo

(a) Data Quality Flag (DQF)

Byte	*Bit*	*Flag*	*Source*	*Description*
0	*0*	*Overall quality*	*Temporal filter*	*0: with retrieval, 1: no retrieval*

(b) Product Quality Information (PQI)

Byte	*Bit*	*Flag*	*Source*	*Description*
0	*0*	*Overall quality*	*Temporal filter*	*0: with retrieval, 1: no retrieval*
	1	*Snow season*	*Climatology*	*0=not in snow season, 1=in snow season*
	2	*High quality retrieval from current day*	*LSA*	*0=with high quality retrieval, 1=no high quality retrieval*
	3-4	*Number of valid retrievals in window*	*LSA*	*00: 0, 01: 1, 10:2-4, 11:>4*
	5	*Quality of climatology data*	*Climatology*	*0: with high quality climatology data , 1:no high quality climatology data*
	6	*SeaIce Flag*	*LSA*	*0: not sea-ice surface; 1: sea-ice surface*
	7	*Reserved*		

* Note: The left-most bit is the most significant bit (the high-order bit) in the definition and description of above PQI and DQF in online/offline albedo.

We designed quality flags for both online and offline LSA algorithm. The quality flags are contained in two layers, Product Quality Information (PQI). Product Control Flags (DQF). The DQF is the concise version for PQI.

2.6.3.2 Metadata list

A series of metadata items were designed to monitor the VIIRS LSA quality. The metadata items are statistics at granule level for online output and at tile level for offline output, which are stored in the netcdf files as variables.

Table 2-9. Metadata list for online VIIRS albedo

Metadata Items	Description
OvQltyHghQltyRtr	Number of High Quality Retrieval
OvQltyRtr	Number of medium Quality Retrieval
OvQltyNoRtr	Number of Invalid Retrieval
CldConfClr	Number of Confidently Clear Pixels
CldProbClr	Number of Probably Clear Pixels
CldProbCld	Number of Probably Cloudly Pixels
CldConfCld	Number of Confidently Cloudy Pixels
RtrPthGen	Number of generic pixels
RtrPthDst	Number of desert pixels
RtrPthSnw	Number of snow pixels
RtrPthSI	Number of sea-ice pixels
RtrPthNoRtr	Number of other pixels
SZAFav	Number of pixels with Favorable SZA
SZALge	Number of pixels with Very Large SZA
VZAFav	Number of pixels with Favorable VZA
VZALge	Number of pixels with Very Large VZA
TFHghRtr	Temporal filtered high quality retrieval
TFDegRtr	Temporal filtered low quality retrieval
TFNoRtr	Temporal filtered no retrieval

OnFltNoFlt	Number of pixels without online simple filtering
OnFltFltd	Number of pixels after online simple filtering
MaxLSA	Maximum Valid Albedo Value
MinLSA	Minimum Valid Albedo Value
MeanLSA	Mean value of Valid Albedo Value
StdLSA	Standard deviation of Valid Albedo Value
PercentHighQuality	OvQltyHghQltyRtr/(TFDegRtr+TFHghRtr)
PercentFilteredPixel	TFDegRtr/ (TFDegRtr+TFHghRtr)
PercentLandPixels	(RtrPthGen+RtrPthSnw+RtrPthDst)/ AllPixelNumber
PercentSeaicePixels	RtrPthSI/ AllPixelNumber
PercentClearPixels	CldConfClr / AllPixelNumber
PercentLargeSZAPixels	VZALge/ AllPixelNumber
PercentLargeVZAPixels	SZALge/ AllPixelNumber

Table 2-10. Metadata list for offline VIIRS albedo

Metadata Items	Description
Overall_Quality:_With_Retrieval	Number of Valid Retrieval
Overall_Quality:_No_Retrieval	Number of Invalid Retrieval
Snow_Season:_Not_in_Snow_Season	Number of Snow Free Pixels
Snow_Season:_In_Snow_Season	Number of Snow Pixels
Retrieval_from_Current_Day:_With_High_ Quality_Retrieval	Number of High Quality Retrieval on Current Day
Retrieval_from_Current_Day:_No_High_Qu ality_Retrieval	Number of Low Quality Retrieval on Current Day
Number_of_Valid_Retrievals_in_Window:_ 0	Number of Pixels Using 0 Valid Retrievals in Filtering
Number_of_Valid_Retrievals_in_Window:_ 1	Number of Pixels Using 1 Valid Retrievals in Filtering
Number_of_Valid_Retrievals_in_Window:_ 2-4	Number of Pixels Using 2-4 Valid Retrievals in Filtering
Number_of_Valid_Retrievals_in_Window:_ >4	Number of Pixels Using more than 4 Valid Retrievals in Filtering

Climatology_Quality:_With_High_Quality_ Climatology	Number of Pixels with High Quality Climatology
Climatology_Quality:_No_High_Quality_Climatology	Number of Pixels with Low Quality Climatology
SeaIce_Flag:_Not_SeaIce_Surface	Number of Pixels not Sea-ice Covered
SeaIce_Flag:_SeaIce_Surface	Number of Pixels with Sea-ice Covered
MaxLSA	Maximum Valid Albedo Value
MinLSA	Minimum Valid Albedo Value
MeanLSA	Mean value of Valid Albedo Value
StdLSA	Standard deviation of Valid Albedo Value

2.6.4 Algorithm Validation

A summary of our previous validation results has been given in Section 2.5. In order to quantify the retrieval errors and improve the inversion algorithm, we need to carry out more extensive validation work. Albedo is continuously measured by several surface measurement networks, such as Atmospheric Radiation Measurement at the Southern Great Plains, SURFRAD, and Ameriflux projects. We have conducted albedo validation extensively during recent years, and will continue this activity for the VIIRS albedo product over more surface types.

3.   ASSUMPTIONS AND LIMITATIONS

The following sections describe the assumptions in developing and estimating the performance of the current version of VIIRS surface albedo algorithm. The limitations and potential algorithm improvement are also discussed.

3.1 Assumptions

The following assumptions have been made in developing the VIIRS surface albedo algorithm:

- Comprehensive database of atmospheric conditions and surface BRDF were used in training the direct estimation algorithm. The database is assumed to be representative.
- Albedo climatology derived from historical albedo data sets was used in temporal filtering. The current albedo values are assumed to follow the statistical distribution and temporal correlation described by the climatology.

3.2 Quality of Upstream Input Data

Accurate estimation of VIIRS surface albedo depends on reliable input of upstream VIIRS data and products, such as TOA reflectance, cloud mask, surface type, snow mask, and sea-ice concentration. In the section of sensitivity analysis, we have demonstrated the importance of some input data products. The temporal filtering algorithm was developed to correct some problems caused by inaccurate input data, such as undetected cloud coverage.

3.3 Algorithm Improvement

The temporal filter can substantially improve estimates of snow-free albedo by filling data gaps and reducing random errors. However, its benefits with regards to ephemeral snow cases are rather limited. Due to large day-to-day albedo variability, temporally neighboring observations are not sufficient for predicting cloudy-day albedo. More sophisticated algorithms are needed that can incorporate information other than optical remote sensing data, such as microwave remote sensing (Xue et al. 2014) and ancillary data sources (i.e., temperature) to infer albedo during cloudy days and to generate a continuous albedo field with improved accuracy.

4. REFERENCES

Arola, A., Eck, T.F., Huttunen, J., Lehtinen, K.E.J., Lindfors, A.V., Myhre, G., Smirnov, A., Tripathi, S.N., & Yu, H. (2013). Influence of observed diurnal cycles of aerosol optical depth on aerosol direct radiative effect. *Atmospheric Chemistry and Physics, 13*, 7895-7901

Baldridge, A.M., Hook, S.J., Grove, C.I., & Rivera, G. (2009). The ASTER spectral library version 2.0. *Remote Sensing of Environment, 113*, 711-715

Berk, A., Anderson, G.P., Acharya, P.K., Bernstein, L.S., Muratov, L., Lee, J., Fox, M., Adler-Golden, S.M., Chetwynd, J.H., Hoke, M.L., Lockwood, R.B., Cooley, T.W., & Gardnerb, J.A. (2004). *MODTRAN5: A Reformulated Atmospheric Band Model with Auxiliary Species and Practical Multiple Scattering Options*.

Bisht, G., Venturini, V., Islam, S., & Jiang, L. (2005). Estimation of the net radiation using MODIS (Moderate Resolution Imaging Spectroradiometer) data for clear sky days. *Remote Sensing of Environment, 97*, 52-67

Bonan, G.B., Oleson, K.W., Vertenstein, M., Levis, S., Zeng, X.B., Dai, Y.J., Dickinson, R.E., & Yang, Z.L. (2002). The land surface climatology of the community land model coupled to the NCAR community climate model. *Journal of Climate, 15*, 3123-3149

Cescatti, A., Marcolla, B., Vannan, S.K.S., Pan, J.Y., Roman, M.O., Yang, X., Ciais, P., Cook, R.B., Law, B.E., Matteucci, G., Migliavacca, M., Moors, E., Richardson, A.D., Seufert, G., & Schaaf, C.B. (2012). Intercomparison of MODIS albedo retrievals and in situ measurements across the global FLUXNET network. *Remote Sensing of Environment, 121*, 323-334

Clark, R.N., Swayze, G.A., Wise, R., Livo, E., Hoefen, T., Kokaly, R., Sutley, S.J. (2007). USGS digital spectral library splib06a. In, *Digital Data Series 231*: U.S. Geological Survey

Csiszar, I., & Gutman, G. (1999). Mapping global land surface albedo from NOAA AVHRR. *Journal of Geophysical Research-Atmospheres, 104*, 6215-6228

Eltahir, E.A.B. (1998). A soil moisture rainfall feedback mechanism 1. Theory and observations. *Water Resources Research, 34*, 765-776

Fang, H., Liang, S., Kim, H.Y., Townshend, J.R., Schaaf, C.L., Strahler, A.H., & Dickinson, R.E. (2007). Developing a spatially continuous 1 km surface albedo data set over North America from Terra MODIS products. *Journal of Geophysical Research-Atmospheres, 112*

Feng, Y., Liu, Q., Qu, Y., & Liang, S. (2016). Estimation of the ocean water albedo from remote sensing and meteorological reanalysis data. *IEEE Transactions On Geoscience And Remote Sensing*, 54, 850-868

Gardner, A.S., & Sharp, M.J. (2010). A review of snow and ice albedo and the development of a new physically based broadband albedo parameterization. *Journal of Geophysical Research: Earth Surface*, 115

Grant, I.F., Prata, A.J., & Cechet, R.P. (2000). The impact of the diurnal variation of albedo on the remote sensing of the daily mean albedo of grassland. *Journal of Applied Meteorology, 39*, 231-244

He, T., Liang, S., Wang, D., Shi, Q., & Tao, X. (2014). Estimation of High-Resolution Land Surface Shortwave Albedo From AVIRIS Data. *IEEE Journal of Selected Topics in Applied Earth Observations and Remote Sensing, 7*, 4919-4928

Holben, B.N., Tanre, D., Smirnov, A., Eck, T.F., Slutsker, I., Abuhassan, N., Newcomb, W.W., Schafer, J.S., Chatenet, B., Lavenu, F., Kaufman, Y.J., Castle, J.V., Setzer, A., Markham, B., Clark, D., Frouin, R., Halthore, R., Karneli, A., O'Neill, N.T., Pietras, C., Pinker, R.T., Voss, K., & Zibordi, G. (2001). An emerging ground-based aerosol climatology: Aerosol optical depth from AERONET. *Journal of Geophysical Research-Atmospheres, 106*, 12067-12097

Kotchenova, S.Y., Vermote, E.F., Levy, R., & Lyapustin, A. (2008). Radiative transfer codes for atmospheric correction and aerosol retrieval: intercomparison study. *Applied Optics, 47*, 2215-2226

Kuusinen, N., Kolari, P., Levula, J., Porcar-Castell, A., Stenberg, P., & Berninger, F. (2012). Seasonal variation in boreal pine forest albedo and effects of canopy snow on forest reflectance. *Agricultural and Forest Meteorology, 164*, 53-60

Li, Z.Q., & Garand, L. (1994). Estimation of surface albedo from space: a parameterization for global application. *Journal of Geophysical Research-Atmospheres, 99*, 8335-8350

Liang, S. (2001). Narrowband to broadband conversions of land surface albedo I Algorithms. *Remote Sensing of Environment, 76*, 213-238

Liang, S. (2003). A direct algorithm for estimating land surface broadband albedos from MODIS imagery. *IEEE Transactions on Geoscience and Remote Sensing, 41*, 136-145

NOAA

VIIRS Surface Albedo Algorithm Theoretical Basis Document
Page 53 of 56

Liang, S. (2004). *Quantitative Remote Sensing of Land Surfaces*. Hoboken: John Wiley & Sons

Liang, S., Strahler, A.H., & Walthall, C. (1999). Retrieval of land surface albedo from satellite observations: A simulation study. *Journal of Applied Meteorology, 38*, 712-725

Liang, S., Zhao, X., Yuan, W., Liu, S., Cheng, X., Xiao, Z., Zhang, X., Liu, Q., Cheng, J., Tang, H., Qu, Y.H., Bai, Y., Qu, Y., Ren, H., Yu, K., & Townshend, J. (2013). A Long-term Global LAnd Surface Satellite (GLASS) Dataset for Environmental Studies. *International Journal of Digital Earth, In press*

Liu, N., Liu, Q., Wang, L., Liang, S., Wen, J., Qu, Y., & Liu, S. (2013a). A statistics-based temporal filter algorithm to map spatiotemporally continuous shortwave albedo from MODIS data. *Hydrology and Earth System Sciences, 17*, 2121-2129

Liu, Q., Wang, L., Qu, Y., Liu, N., Liu, S., Tang, H., & Liang, S. (2013b). Preliminary evaluation of the long-term GLASS albedo product. *International Journal of Digital Earth, 6*, 69-95

Loarie, S.R., Lobell, D.B., Asner, G.P., & Field, C.B. (2011). Land-Cover and Surface Water Change Drive Large Albedo Increases in South America. *Earth Interactions, 15*, 1-16

Long, D., Gao, Y., & Singh, V.P. (2010). Estimation of daily average net radiation from MODIS data and DEM over the Baiyangdian watershed in North China for clear sky days. *Journal of Hydrology, 388*, 217-233

Loranty, M.M., Goetz, S.J., & Beck, P.S.A. (2011). Tundra vegetation effects on pan-Arctic albedo. *Environmental Research Letters, 6*

Lucht, W., Schaaf, C.B., & Strahler, A.H. (2000). An algorithm for the retrieval of albedo from space using semiempirical BRDF models. *IEEE Transactions on Geoscience and Remote Sensing, 38*, 977-998

Manninen, T., Riihela, A., & de Leeuw, G. (2012). Atmospheric effect on the ground-based measurements of broadband surface albedo. *Atmospheric Measurement Techniques, 5*, 2675-2688

Moody, E.G., King, M.D., Platnick, S., Schaaf, C.B., & Gao, F. (2005). Spatially complete global spectral surface albedos: Value-added datasets derived from terra MODIS land products. *IEEE Transactions on Geoscience and Remote Sensing, 43*, 144-158

Morassutti, M. P., and E. F. LeDrew. "Albedo and depth of melt ponds on sea‐ice." International Journal of Climatology: *A Journal of the Royal Meteorological Society* 16.7 (1996): 817-838.

Offerle, B., Grimmond, C.S.B., & Oke, T.R. (2003). Parameterization of net all-wave radiation for urban areas. *Journal of Applied Meteorology, 42*, 1157-1173

Peng, J., Liu, Q., Wen, J., Liu, Q., Tang, Y., Wang, L., ... & Feng, Y. (2015). Multi-scale validation strategy for satellite albedo products and its uncertainty analysis. *Science China Earth Sciences, 58*, 573-588.

Qu, Y., Liang, S., Liu, Q., Li, X., Feng, Y., & Liu, S. (2016). Estimating Arctic sea-ice shortwave albedo from MODIS data. *Remote Sensing of Environment, 186*, 32-46

Qu, Y., Liu, Q., Liang, S., Wang, L., Liu, N., & Liu, S. (2014). Direct-Estimation Algorithm for Mapping Daily Land-Surface Broadband Albedo From MODIS Data. *IEEE Transactions on Geoscience and Remote Sensing, 52*, 907-919

Radhakrishna, B., Fabry, F., Braun, J.J., & Van Hove, T. (2015). Precipitable Water from GPS over the Continental United States: Diurnal Cycle, Intercomparisons with NARR, and Link with Convective Initiation. *Journal of Climate, 28*, 2584-2599

Raschke, E., Vonderha.Th, Bandeen, W.R., & Pasterna.M (1973). Annual radiation balance of Earth-atmophere system during 1969-70 from Nimbus-3 measurements. *Journal of the Atmospheric Sciences, 30*, 341-364

Riihela, A., Manninen, T., Laine, V., Andersson, K., & Kaspar, F. (2013). CLARA-SAL: a global 28 yr timeseries of Earth's black-sky surface albedo. *Atmospheric Chemistry and Physics, 13*, 3743-3762

Román, M.O., Schaaf, C.B., Lewis, P., Gao, F., Anderson, G.P., Privette, J.L., Strahler, A.H., Woodcock, C.E., & Barnsley, M. (2010). Assessing the coupling between surface albedo derived from MODIS and the fraction of diffuse skylight over spatially-characterized landscapes. *Remote Sensing of Environment, 114*, 738-760

Rutan, D., Rose, F., Roman, M., Manalo-Smith, N., Schaaf, C., & Charlock, T. (2009). Development and assessment of broadband surface albedo from Clouds and the Earth's Radiant Energy System Clouds and Radiation Swath data product. *Journal of Geophysical Research-Atmospheres, 114*

Rutan, D.A., Smith, G.L., & Wong, T.M. (2014). Diurnal Variations of Albedo Retrieved from Earth Radiation Budget Experiment Measurements. *Journal of Applied Meteorology and Climatology, 53*, 2747-2760

Schaaf, C.B., Gao, F., Strahler, A.H., Lucht, W., Li, X.W., Tsang, T., Strugnell, N.C., Zhang, X.Y., Jin, Y.F., Muller, J.P., Lewis, P., Barnsley, M., Hobson, P., Disney, M., Roberts, G., Dunderdale, M., Doll, C., d'Entremont, R.P., Hu, B.X., Liang, S., Privette, J.L., & Roy, D. (2002). First operational BRDF, albedo nadir reflectance products from MODIS. *Remote Sensing of Environment, 83*, 135-148

Stamnes, K., Hamre, B., Stamnes, J.J., Ryzhikov, G., Biryulina, M., Mahoney, R., Hauss, B., & Sei, A. (2011). Modeling of radiation transport in coupled atmosphere-snow-ice-ocean systems. *Journal of Quantitative Spectroscopy and Radiative Transfer*, 112, 714-726

Tian, B.J., Soden, B.J., & Wu, X.Q. (2004). Diurnal cycle of convection, clouds, and water vapor in the tropical upper troposphere: Satellites versus a general circulation model. *Journal of Geophysical Research-Atmospheres, 109*

Townshend, J.R.G., & Justice, C.O. (2002). Towards operational monitoring of terrestrial systems by moderate-resolution remote sensing. *Remote Sensing of Environment, 83*, 351-359

Vermote, E.F., Tanré, D., Deuze, J.L., Herman, M., & Morcette, J. (1997). Second simulation of the satellite signal in the solar spectrum, 6S: An overview. *IEEE Transactions On Geoscience and Remote Sensing*, 35, 675-686

Vermote, E., Justice, C., & Csiszar, I. (2014). Early evaluation of the VIIRS calibration, cloud mask and surface reflectance Earth data records. *Remote Sensing of Environment, 148*, 134-145

Wang, D., Liang, S., He, T., & Yu, Y. (2013). Direct estimation of land surface albedo from VIIRS data: Algorithm improvement and preliminary validation. *Journal of Geophysical Research-Atmospheres, 118*, 12577-12586

Wang, D., Liang, S., He, T., Yu, Y., Schaaf, C., & Wang, Z. (2015). Estimating daily mean land surface albedo from MODIS data. *Journal of Geophysical Research-Atmospheres, 120*, 4825-4841

Wang, D., Liang, S., Zhou, Y., He, T., & Yu, Y. (2017). A new method for retrieving daily land surface albedo from VIIRS data. *IEEE Transactions on Geoscience and Remote Sensing, 55*, 1765 - 1775

Wang, Z., Barlage, M., Zeng, X.B., Dickinson, R.E., & Schaaf, C.B. (2005). The solar zenith angle dependence of desert albedo. *Geophysical Research Letters, 32*

Xue, H., Wang, J., Xiao, Z., Chen, P., & Liu, Y. (2014). Combining MODIS and AMSR-E observations to improve MCD43A3 short-time snow-covered Albedo estimation. *Hydrological Processes, 28*, 570-580

Zege, E., Malinka, A., Katsev, I., Prikhach, A., Heygster, G., Istomina, L., Birnbaum, G., & Schwarz, P. (2015). Algorithm to retrieve the melt pond fraction and the spectral albedo of Arctic summer ice from satellite optical data. *Remote Sensing Of Environment*, 163, 153-164

Zhang, X., Liang, S., Wang, K., Li, L., & Gui, S. (2010). Analysis of Global Land Surface Shortwave Broadband Albedo From Multiple Data Sources. *IEEE Journal of Selected Topics in Applied Earth Observations and Remote Sensing, 3*, 296-305

Zheng, X.Y., & Eltahir, E.A.B. (1998). A soil moisture rainfall feedback mechanism 2. Numerical experiments. *Water Resources Research, 34*, 777-785

Zhou, Y., Wang, D., Liang, S., Yu, Y., & He, T. (2016). Assessment of the Suomi NPP VIIRS Land Surface Albedo Data Using Station Measurements and High -Resolution Albedo Maps. *Remote Sensing, 8*

Zhu, X., Liang, S., Pan, Y., & Zhang, X. (2011). Agricultural Irrigation Impacts on Land Surface Characteristics Detected From Satellite Data Products in Jilin Province, China. *IEEE Journal of Selected Topics in Applied Earth Observations and Remote Sensing, 4*, 721-729

END OF DOCUMENT